Josephson effects in twisted nodal superconductors

Pavel A. Volkov [1,2,3,*] S. Y. Frank Zhao [3] Nicola Poccia [4] Xiaomeng Cui [3] Philip Kim [3] and J. H. Pixley [2]

[1]*Department of Physics, University of Connecticut, Storrs, Connecticut 06269, USA*

[2]*Department of Physics and Astronomy, Center for Materials Theory, Rutgers University, Piscataway, New Jersey 08854, USA*

[3]*Department of Physics, Harvard University, Cambridge, Massachusetts 02138, USA*

[4]*Leibniz Institute for Solid State and Materials Science Dresden (IFW Dresden), 01069 Dresden, Germany*

(Received 10 September 2021; revised 12 November 2024; accepted 26 November 2024; published 21 January 2025)

Motivated by the recent proposals for unconventional emergent physics in twisted bilayers of nodal superconductors, we study the peculiarities of the Josephson effect at the twisted interface between d-wave superconductors. We demonstrate that for clean interfaces with a twist angle θ_0 in the range $0^\circ < \theta_0 < 45^\circ$, the critical current can exhibit nonmonotonic temperature dependence with a maximum at a nonzero temperature as well as a complex dependence on the twist angle at low temperatures. These effects are shown to reflect the destructive interference between the d-wave order parameters near the nodes at nonzero twist angle. Close to $\theta_0 = 45^\circ$ we find that the critical current does not vanish due to Cooper pair cotunneling, which can lead to the transition to a time-reversal breaking superconducting $d + id$ phase, which can be suppressed by the interface roughness. We provide a comprehensive theoretical analysis of experiments that can reveal this cotunneling for twisted superconductors close to $\theta_0 = 45^\circ$. In particular, we demonstrate that both the emergence of the Fraunhofer interference pattern near $\theta_0 = 45^\circ$ and fractional Shapiro steps yield unambiguous evidence of Cooper pair cotunneling, necessary for topological superconductivity.

DOI: 10.1103/PhysRevB.111.014514

I. INTRODUCTION

Experiments on two-dimensional (2D) materials have reached an unprecedented level of control and precision. 2D sheets of atomically thin layers can be isolated via exfoliation and stacked to make a wide range of devices [1]. This approach is expected to be applicable to a variety of materials [2] that can be exfoliated, i.e., have binding energy densities less than $\sim$100 meV Å^{-2}. With the development of the "tear and stack" approach [3], it is now possible to accurately control the twist angle (to within $\sim 0.1^\circ$) between sheets of a variety of 2D materials, such as boron nitride [4,5], graphene [6–14], and transition-metal dichalcogenides [15–17]. The superlattice generated due to the moiré pattern that is realized due to the twist downfolds and strongly renormalizes the single-particle spectrum [18–21]. This approach has successfully led to the observation of correlated insulators and superconductors across a wide range of devices ushering in a new era of "twistronics" [22] or "moiré materials" [23]. Developing a theoretical description for the resulting single-particle excitations and their instability to interactions has attracted a great deal of theoretical attention [20,24–37].

The strongly correlated high-temperature cuprate superconductors are layered materials with a highly anisotropic quasi-two-dimensional layered structure [38]. This has recently led to the realization of atomically thin sheets [39–41] of $Bi_2Sr_2CaCu_2O_{8+x}$ (BSCCO) with superconducting transition temperatures very close to that measured in bulk samples. These findings in conjunction with the recent success of moiré materials [42] have partly motivated theoretical proposals to twist nodal superconductors, at small [43,44] and large twist angles [45,46]. In the case of singlet d-wave superconductors, small twist angles $\theta_0 \approx 1^\circ$ can possess a magic angle in the Bogoliubov–de Gennes spectrum that drives strong interactions between the quasiparticles, whereas at large twist angles (in particular $\theta_0 = 45^\circ$) the free energy of the system is lowered by spontaneously generating a phase difference between the two layers, breaking time reversal symmetry (TRSB). In this regime, a $d + id$ topological superconducting ground state is realized with a Josephson current-phase ($I - \varphi$) relation between the bilayers that is fundamentally altered [47] from $I \sim \sin\varphi$ to $I \sim \sin 2\varphi$.

Recent experiments on exfoliated thin slabs of BSCCO homojunctions with atomically abrupt interfaces have successfully realized twisted devices with a critical current that strongly depends on the twist angle [48–50]. In these devices, BSCCO was cooled to cryogenic temperatures during stacking, which preserved the interfacial structure and superconductivity. In contrast, all the previous experimental attempts to realize superconducting interfaces along the c axis with BSCCO required annealing at high temperature [51–53] and yielded varying results on the twist dependence of the critical current. In particular, the strong suppression of the critical current (to zero in the lowest order in tunneling [54,55]) has been observed only in one experiment [52]. On the other hand, the cryogenically prepared twist junctions [48–50] demonstrate a dramatic suppression of critical current towards 45°, as well as an interesting nonmonotonic dependence of the critical current. Near 45°, such twisted junctions exhibit fractional

*Contact author: pavel.volkov@uconn.edu

Shapiro steps and a modified Fraunhofer pattern [48], indicating that the Josephson current-phase relation is consistent with the second harmonic.

In a range around 45°, the twisted BSCCO junctions were also shown to exhibit a trainable superconducting diode effect [48,56], demonstrating the emergence of time-reversal broken superconductivity at the interface. All of these observations taken together provide the necessary symmetry conditions for the system to realize topological superconductivity in bilayers [43,46] or flakes containing a finite number of layers [57,58]. However, to date "smoking gun" experimental evidence of topology, such as the quantized thermal Hall effect (κ_{xy}/T), has not been observed.

This experimental breakthrough necessitates the development of a detailed theoretical description of the temperature and twist angle dependence of the critical current as well as the emergent behavior of twisted nodal superconductor interfaces in magnetic fields that goes beyond the previous works [54,55,59]. In particular, a possible nonmonotonic temperature dependence of the critical current or signatures of a topological phase near $\theta_0 = 45°$, including magnetic field effects, has not been studied.

In this manuscript, we develop a theoretical description of the Josephson effect at interfaces between twisted slabs of nodal superconductors. We use the tunneling Hamiltonian approach for a detailed study of how the critical current depends on temperature, twist angle, and magnetic field, including the effects of interface inhomogeneity and higher-order tunneling processes. For clean and regular interfaces, we show that the temperature dependence of the critical current reflects the Fermi surface geometry and the form of the interlayer tunneling, which generally leads to a nonmonotonic dependence on temperature and twist angle. The presence of nanoscale inhomogeneities at the twist interface washes out the finer details, leading to a critical current that goes like $I_c \sim \cos(2\theta_0)$ away from $\theta_0 = 45°$. For twist angles close to $\theta_0 = 45°$, the critical current is mediated by the cotunneling of Cooper pairs that can lead to the realization of a topological time-reversal breaking $d + id$ superconducting state with a current-phase relationship that is given by the second harmonic. For increasing inhomogeneity roughness, we find that the topological superconducting phase is destroyed and time-reversal symmetry restored. Using the derived twist angle-dependent critical current, the effects of a parallel magnetic field are investigated while incorporating the realistic device geometry used in recent experiments [48]. As a result, we are able to demonstrate the emergence of the Fraunhofer pattern of the critical current close to $\theta_0 = 45°$ and show how it can be used to reveal the current-phase relationship of the twist junction. Lastly, we study the effects of a microwave drive on the twist junction and show that the presence of fractional Shapiro steps as well as the properties of the width of each step can be used to characterize the contribution of cotunneling, necessary for topological superconductivity near $\theta_0 = 45°$.

The remainder of the paper is organized as follows. In Sec. II we discuss the model investigated and general relations used to compute the current. In Sec. III we study the effects of Fermi surface geometry and momentum-dependent tunneling with a clean interface where translational symmetry is preserved, and in Sec. IV we determine how these conclusions are altered by considering momentum relaxation due to nanoscale inhomogeneities breaking translational symmetry at the interface. The computed critical current as a function of temperature and twist angle is used to determine the behavior of the critical current in the presence of a magnetic field, including emergent Fraunhofer patterns, as well the structure of Shapiro steps in the presence of microwave drive in Sec. V. We conclude in Sec. VI.

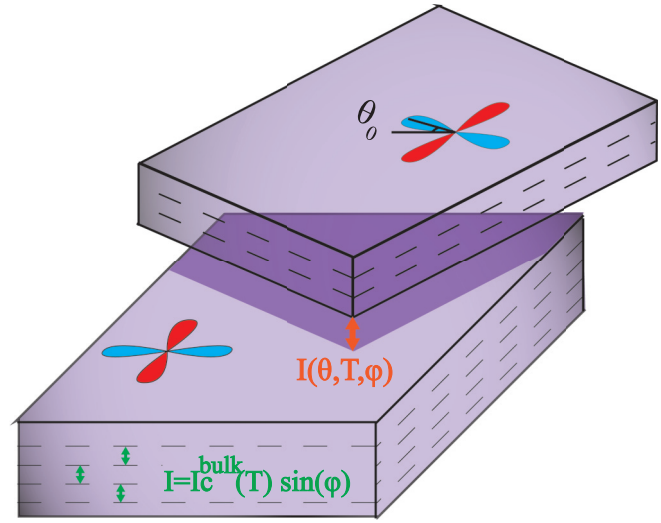

FIG. 1. Twisted interfaces between nodal superconductors. The schematic shows two finite-thickness flakes of a highly two-dimensional d-wave superconductor. In the bulk of the flakes, individual layers (dashed lines) are coupled by a conventional Josephson tunneling, while at the interface the current-phase relation can depend on the twist angle θ_0.

II. MODEL AND GENERAL RELATIONS

The recent twisted BSCCO Josephson junction experiments [48–50,60] are performed on devices consisting of two flakes of finite thickness, each consisting of a large number of BSCCO unit cells along the c axis (Fig. 1). It is established [61,62] that in bulk BSCCO, the coupling between the superconducting order parameters between the neighboring CuO_2 bilayers can be well described by a conventional Josephson coupling. Consequently, when describing twisted flakes of finite thickness, we will use the effective model of Josephson coupled layers, where coupling between all the layers except at the twisted interface reduces to the conventional Josephson coupling. In the following section, we describe the microscopic approach used to compute the interlayer supercurrent across the twisted interface and its dependence on the phase difference of two superconducting bilayers, the temperature and the twist angle.

A. Effective model at the interface

We start with a model of a superconducting layer with the second layer twisted at an angle θ_0 with respect to the first one. As we will treat the interlayer tunneling as perturbation, the Josephson coupling between the layers at the interface and the neighboring layers within each flake can be evaluated

independently. We will also neglect the coupling between layers that are not nearest neighbors assuming the tunneling to be weak. Finally, we will assume macroscopically large interfaces, such that the edge contributions to the effects discussed here can be neglected. A potential contribution of edge modes in the topological state is one such contribution, which is expected to be subleading in the junction size. A pair of superconducting layers are described by the Hamiltonian

$$\hat{H} = \sum_{\mathbf{k},s} \xi(\mathbf{k}) c^{\dagger}_{\mathbf{k}s1} c_{\mathbf{k}s1} + \xi(\tilde{\mathbf{k}}) c^{\dagger}_{\mathbf{k}s2} c_{\mathbf{k}s2} + \sum_{\mathbf{k}} [\Delta(\mathbf{k}, T) \times e^{i\varphi} c^{\dagger}_{\mathbf{k}\uparrow 1} c^{\dagger}_{-\mathbf{k}\downarrow 1} + \Delta(\tilde{\mathbf{k}}, T) c^{\dagger}_{\mathbf{k}\uparrow 2} c^{\dagger}_{-\mathbf{k}\downarrow 2} + \text{H.c.}], \quad (1)$$

where $\tilde{\mathbf{k}} = R_{\theta_0}\mathbf{k}$, R_{θ_0} being a rotation matrix around the z axis, $\xi(\mathbf{k})$ is the single-particle dispersion, and $\Delta(\mathbf{k}, T)e^{i\varphi} \equiv \Delta_1(\mathbf{k}, T)$ and $\Delta(\tilde{\mathbf{k}}, T) \equiv \Delta_2(\tilde{\mathbf{k}}, T)$ are the superconducting order parameters in layer one and two, respectively, with φ being the phase difference between the two. For the tunneling between the two layers, we assume spin-independent single-particle tunneling and follow the approach of Refs. [19,43,44], writing the tunneling in momentum space:

$$\hat{H}_{\text{tun}} = \sum_{\mathbf{k},\mathbf{k}',s} t(\mathbf{k}, \mathbf{k}') c^{\dagger}_{\mathbf{k}s1} c_{\mathbf{k}'s2} + \text{H.c.}, \quad (2)$$

where the rotation is accounted for by (1). Equation (2) represents the most general form of the tunneling Hamiltonian. We note that by keeping the tunneling matrix element dependent on momenta in both layers, we can consider both the situations where the in-plane momentum is conserved (corresponding to a clean interface) and is not conserved (due to the moiré quasiperiodicity, roughness, and disorder at the twisted interface). For a clean system, the tunneling is momentum-conserving, $t(\mathbf{k}, \tilde{\mathbf{k}}') = t(\mathbf{k} + \mathbf{G})\delta_{\mathbf{k}+\mathbf{G},\tilde{\mathbf{k}}'}$, where $\mathbf{G}$ is a reciprocal-lattice vector [19]. In what follows, we will ignore the umklapp processes generated by $G \neq 0$ in the clean case. These processes can be rigorously ignored for a Fermi surface being close to the Γ point [43,44]. While they can be of the same order close to the Brillouin zone edge, we will ignore them in the main text for a qualitative assessment of the tunneling and assess their influence in Appendix E. The results there show that allowing for such processes does not significantly change the results if the tunneling decays as a function of momentum on scales of the order of a reciprocal-lattice vector $|\mathbf{G}|$, as expected in twisted bilayers that are weakly bonded (i.e., the lattice constant along the c axis is larger than in the plane) [19].

To study the Josephson effects in the twisted bilayer, we use the general expression for the current-phase relation (CPR) (valid regardless of the tunneling strength) [63]

$$I(\varphi) = \frac{2e}{\hbar}\frac{dF(T,\varphi)}{d\varphi}, \quad (3)$$

where the free energy is given by

$$F(T, \theta_0, \varphi) = -T \text{Tr} \log[\hat{G}^{-1}(i\varepsilon_n, \mathbf{k})\delta_{\mathbf{k},\mathbf{k}'} - \hat{t}(\mathbf{k}, \mathbf{k}')] \quad (4)$$

and

$$\hat{G}^{-1}(i\varepsilon_n, \mathbf{k}) = i\varepsilon_n - \begin{bmatrix} \xi(\mathbf{k})\tau_3 + \Delta(\mathbf{k})[\cos\varphi\tau_1 - \sin\varphi\tau_2] & 0 \\ 0 & \xi(\tilde{\mathbf{k}})\tau_3 + \Delta(\tilde{\mathbf{k}})\tau_1 \end{bmatrix}, \quad \hat{t}(\mathbf{k}, \mathbf{k}') = \begin{bmatrix} 0 & t(\mathbf{k}, \mathbf{k}')\tau_3 \\ t^*(\mathbf{k}, \mathbf{k}')\tau_3 & 0 \end{bmatrix}, \quad (5)$$

where the matrices act in the layer space.

For the case of weak tunneling, general expressions can be obtained for $I(\varphi, \theta_0, T)$ by expanding the free energy in $t(\mathbf{k}, \mathbf{k}')$. The lowest-order term reads

$$I^{(2)}(\varphi, T, \theta_0) = \frac{2e}{\hbar}\text{Tr}\left[\frac{\partial \hat{G}}{\partial\varphi}\hat{t}\hat{G}\hat{t}\right] = \frac{4e}{\hbar}T\sum_{\varepsilon_n,\mathbf{k},\mathbf{k}'} \frac{|t(\mathbf{k}, \mathbf{k}')|^2\Delta(\mathbf{k})\Delta(\tilde{\mathbf{k}}')\sin\varphi}{\left[\varepsilon_n^2 + \xi^2(\mathbf{k}) + \Delta^2(\mathbf{k})\right]\left[\varepsilon_n^2 + \xi^2(\tilde{\mathbf{k}}') + \Delta^2(\tilde{\mathbf{k}}')\right]} \equiv I_c^{(2)}(T, \theta_0)\sin\varphi, \quad (6)$$

where $\tilde{\mathbf{k}}' = R_{\theta_0}\mathbf{k}'$, and we have introduced the second-order contribution in t to the critical current $I_c^{(2)}$ via the CPR. This result for the current and the CPR corresponds to the conventional linear response obtained from the Kubo formula. Importantly, for $\theta_0 = 45°$, the expression in Eq. (6) vanishes by symmetry for a d-wave superconductor. This can be seen by considering the transformations $x \to -x$ or $y \to -y$. Under these mirror symmetries, $\Delta(\tilde{\mathbf{k}})$ changes sign while $\Delta(\mathbf{k})$ does not, leading to $I^{(2)}(\varphi, T, 45°) = 0$. Note that this statement is still valid for the actual point group of BSCCO crystals [55]. Therefore, for twists close to 45°, the next order in tunneling becomes the leading one. In contrast, higher-order corrections (sixth order and beyond) will always remain subleading to the fourth-order contribution and will be neglected in what follows.

The next order in the expansion is given by

$$\begin{aligned} I^{(4)}(\varphi, T, \theta_0) &= \frac{2e}{\hbar}\text{Tr}\left[\frac{\partial \hat{G}}{\partial\varphi}\hat{t}\hat{G}\hat{t}\hat{G}\hat{t}\hat{G}\hat{t}\right] \\ &= -\frac{8e}{\hbar}T\sum_{\varepsilon_n,\mathbf{k}_1,\tilde{\mathbf{k}}_2,\mathbf{k}_3,\tilde{\mathbf{k}}4} \frac{t(\mathbf{k}_1,\mathbf{k}_2)t(\mathbf{k}_2,\mathbf{k}_3)t(\mathbf{k}_3,\mathbf{k}_4)t(\mathbf{k}_4,\mathbf{k}_1)\sin\varphi}{\left[\varepsilon_n^2 + \xi^2(\mathbf{k}_1) + \Delta^2(\mathbf{k}_1)\right]\left[\varepsilon_n^2 + \xi^2(\tilde{\mathbf{k}}_2) + \Delta^2(\tilde{\mathbf{k}}_2)\right]} \\ &\quad \times \frac{\Delta(\mathbf{k}_1)\Delta(\tilde{\mathbf{k}}_2)\left[\varepsilon_n^2 - \xi(\mathbf{k}_3)\xi(\tilde{\mathbf{k}}_4) + \Delta(\mathbf{k}_3)\Delta(\tilde{\mathbf{k}}_4)\cos\varphi\right]}{\left[\varepsilon_n^2 + \xi^2(\mathbf{k}_3) + \Delta^2(\mathbf{k}_3)\right]\left[\varepsilon_n^2 + \xi^2(\tilde{\mathbf{k}}_4) + \Delta^2(\tilde{\mathbf{k}}_4)\right]} \\ &\equiv I_{1,c}^{(4)}(T, \theta_0)\sin\varphi + I_{2,c}^{(4)}(T, \theta_0)\sin 2\varphi, \end{aligned} \quad (7)$$

where we assumed time-reversal symmetry in the tunneling matrix element [$t(\mathbf{k},\mathbf{k}') = t^*(\mathbf{k},\mathbf{k}')$]. Two features can be noted in this expression: First, its relative minus sign with respect to Eq. (6). Second, the dependence on the phase difference in Eq. (7) contains both first $\sim\sin\varphi$ and second $\sim 2\sin\varphi\cos\varphi = \sin 2\varphi$ harmonic dependence on the phase difference, which allows us to define the fourth-order contribution in t to the critical current in the first $I_{1,c}^{(4)}$ and second $I_{2,c}^{(4)}$ harmonic CPRs. Note that the pure first harmonic term has the same properties under mirror symmetries as Eq. (6) and hence vanishes exactly at $\theta_0 = 45^\circ$. On the other hand, close to T_c, one observes that the $\sin 2\varphi$ term contains an additional square of the order parameter. Consequently, one can expect that at $\theta_0 \neq 45^\circ$, the conventional $\sim\sin\varphi$ harmonic will be dominant close to T_c. Finally, one observed that Eqs. (6) and (7) will depend differently on the overall amplitude of the tunneling—quadratically and quartically, respectively. This suggests that the effects of the second-harmonic contribution (which is quartic in tunneling) will become more important with increasing tunneling amplitude that may depend on, e.g., interface quality or applied pressure.

B. Temperature dependence of the superconducting gap

To study the temperature dependence of the CPR, the temperature dependence of the gap Δ has to be included. As we are interested in the qualitative character of this dependence, we will introduce several simplifying assumptions.

First, we assume a weak coupling between the layers, such that the influence of the interlayer hopping [43,44] and interaction on the magnitude of the mean-field order parameter can be neglected. It follows then that the amplitudes of the order parameters in two layers are independent and equal to each other, i.e., $|\Delta_1| = |\Delta_2| = \Delta$. Note that this does not necessarily imply that the effects of higher-order interlayer tunneling are always negligible for the CPR, and the exact Eqs. (3) and (4) can be used to study those.

The self-consistency equation for the superconducting gap within a single layer then takes the form

$$\Delta(T,\mathbf{k}) = T\sum_{\varepsilon_n,\mathbf{k}'} V_{\rm SC}(\mathbf{k},\mathbf{k}')\frac{\Delta(T,\mathbf{k}')}{\varepsilon_n^2 + \xi^2(\mathbf{k}') + |\Delta(T,\mathbf{k}')|^2}, \quad (8)$$

where $V_{\rm SC}(\mathbf{k},\mathbf{k}')$ is the intralayer pairing interaction. We will further simplify it by taking an instantaneous interaction with a separable form, i.e., $V_{\rm SC}(\mathbf{k},\mathbf{k}') = V_{\rm SC} f(\mathbf{k}) f(\mathbf{k}')$, where $f(\mathbf{k})$ vanishes at the nodes. The solution of (8) is then given by

$$\Delta(T,\mathbf{k}) = \Delta_0(T) f(\mathbf{k}). \quad (9)$$

Finally, we expand $\xi(\mathbf{k})$ and $f(\mathbf{k})$ in Fourier series in the polar angle in momentum space,

$$\theta = \arctan(k_y/k_x), \quad (10)$$

and leave only the lowest harmonics for both. In the rest of the manuscript, we will only focus on the case of a d-wave superconductor (that is relevant for twisted BSCCO). In this case, leaving the lowest angular harmonics only we have $\xi(\mathbf{k}) \to \xi_0(|\mathbf{k}|)$ and

$$f(\mathbf{k}) \to f_0(|\mathbf{k}|)\cos 2\theta. \quad (11)$$

The integration in (8) can be carried out around $k \approx k_F$ such that $f_0(|\mathbf{k}|) \approx f_0(k_F)$. One can then define the superconducting gap amplitude at the Fermi level

$$\Delta(T) \equiv \Delta_0(T) f_0(k_F). \quad (12)$$

Using Eq. (8) at T_c to eliminate $V_{\rm SC}$ in favor of T_c, one arrives at the equation for $\Delta(T)$,

$$\sum_{n=-\infty}^{\infty}\int_0^{2\pi} d\theta\left[\frac{\cos^2 2\theta}{\sqrt{(2n+1)^2 + \frac{|\Delta(T)|^2\cos^2 2\theta}{\pi^2 T^2}}} - \frac{\cos^2 2\theta}{|2n+1|}\right] = 0. \quad (13)$$

In what follows, we use the numerical solution of Eq. (13) for the temperature dependence of the gap amplitude. For numerical summation here and in what follows, $|n| < |n|_{\max} = 20(T_c/T) + 50$, which has been checked to be enough for the sum to converge.

III. $I_c(\theta_0, T)$ FOR COHERENT TUNNELING

In this section, we demonstrate that momentum-conserving tunneling results in the unconventional twist angle- and temperature dependence of the critical current. In particular, we show that both the anisotropy of the gap and the Fermi surface result in strong deviations of the low-temperature $I_c(\theta_0)$ from the $\cos 2\theta_0$ form, which is the lowest harmonic consistent with d-wave symmetry. These deviations appear much stronger than those observed in recent experiments [48] at any temperature. Moreover, the sign-changing nature of the gap is shown to yield a nonmonotonic temperature dependence of I_c at sufficiently large twist angles, consistent with experimental observations [48].

A. Circular Fermi surface

We consider first the simplified model on a circular Fermi surface for $\xi(\mathbf{k}) = v_F(k - k_f)$ and a d-wave gap symmetry $\Delta(\mathbf{k}) = \Delta(T)\cos 2\theta$. We begin by discussing the lowest-order term in the expansion of the CPR in t, Eq. (6). In Fig. 2(a) we present the resulting critical current $I_c^{(2)}(T,\theta_0)$ as a function of twist angle for several temperatures. Close to T_c, one can expand Eq. (6) in the order parameter, resulting in the lowest order in $I_c^{(2)} \sim \int d\theta\,\Delta(\theta)\Delta(\theta+\theta_0) \sim \cos 2\theta_0$. However, at low temperatures [Fig. 2(a)], the twist angle dependence deviates strongly from the $\cos 2\theta_0$ form expected near T_c. The reason for this deviation is the higher harmonics of $\cos 2\theta_0$ appearing in the denominator of Eq. (6) due to the development of an anisotropic d-wave gap.

In the region $\theta_0 \gtrsim 10^\circ$, one also observes that the curve for $T/T_c = 0.25$ lies above the one for $T = 0$. This demonstrates a decrease of $I_c^{(2)}(T,\theta_0)$ on cooling, i.e., a nonmonotonic temperature dependence. We illustrate this in Fig. 2(b), where indeed $I_c^{(2)}(T,\theta_0)$ has a maximum at an intermediate temperature. For large twist angles around 45°, the behavior changes very little, despite the change of the critical current magnitude shown in Fig. 2(a). We note that a nonmonotonic temperature dependence has also been predicted for in-plane d/d junctions [64,65].

Moving towards the next order in the expansion, however, results in a difficulty. It can be observed that the sums in

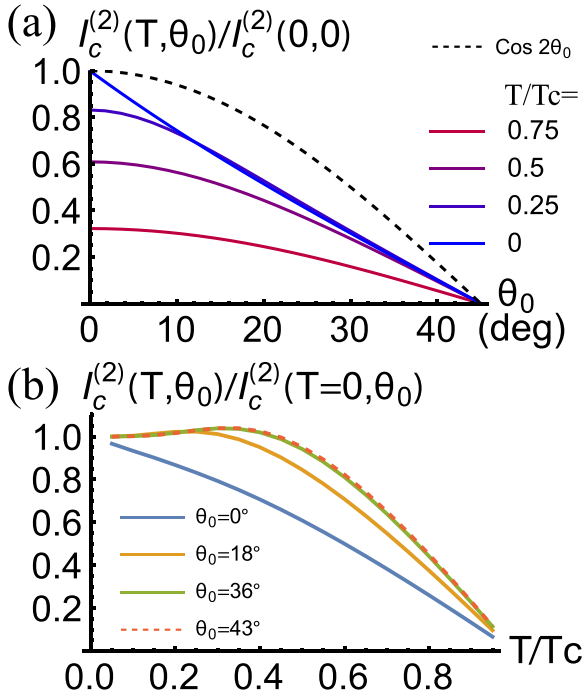

FIG. 2. Second-order approximation of the critical current $I_c^{(2)}(T,\theta_0)$ in Eq. (6) for a circular Fermi surface. Part (a) displays the twist angle θ_0 dependence of $I_c^{(2)}$ differing strongly from the $\cos(2\theta_0)$ behavior for various values of the temperature. (b) The temperature T dependence of $I_c^{(2)}$ for various twist angles that displays a nonmonotonic behavior.

the perturbative expansion at fourth order in Eq. (7) diverge at $\theta_0 = 0$ as $\sim 1/T$ for low temperatures in the vicinity of the Dirac nodes $\Delta(\mathbf{k}) = 0$ and $k = k_F$. This suggests that close to 0° one should use the full expressions, Eqs. (3) and (4), to evaluate the critical current. The tunneling splits two Dirac cones in momentum space at $\theta_0 = 0$ (due to bonding/antibonding band formation), and away from $\theta_0 = 0$ the spectrum is gapped for $\varphi \neq 0$ [43,44], indicating that the divergence is absent in the full formulation. On the other hand, the full current is a rather complicated function of φ which has to be maximized to obtain the critical current. Here we take the following approach: away from $\theta_0 = 0$, we use the expansion in Eqs. (6) and (7) to determine $\varphi_{\max}$ and use it in the full expression for the CPR in Eqs. (3) and (4) for $T/T_c \geqslant 0.05$. At low twist angles, the corrections to the CPR from higher-order tunneling can still be shown to be small for weak tunneling [43,44], while at large twist angles Eq. (7) is not divergent at low T, which justifies taking the perturbative approach to determine $\varphi_{\max}$. Additionally, since the gap opened by the phase difference [43,44] will generally change the low-temperature behavior of the gap from T^3, following from Eq. (13) to an exponential one, we focus on the twist angle dependence at low T. In Fig. 3 we present the twist angle dependence of the critical current compared to the second-order expansion result for $t/T_c = 0.5$ and $T/T_c = 0.05$. Away from $\theta_0 = 45°$, one observes almost no difference between the two, suggesting that the second-order expansion constitutes a good approximation. However, while Eq. (6) manifestly goes to zero at $\theta_0 = 45°$ by symmetry, the full critical current does

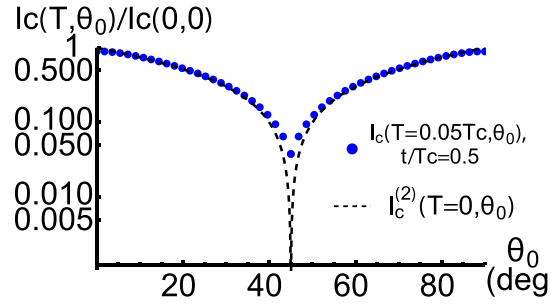

FIG. 3. The twist angle dependence of the normalized critical current defined in Eq. (3) for a circular Fermi surface. Here we take as a representative case $t/T_c = 0.5$ and $T/T_c = 0.05$ and show the data on a log-scale. The dashed line shows the second-order result (6) at $T = 0$ for comparison.

not. This yields a qualitative explanation of the observation of a nonzero critical current at $\theta_0 = 45°$ in the otherwise strongly angle-dependent results of Refs. [48–50,60].

B. Cupratelike Fermi surface

We now consider the qualitative effects of a noncircular Fermi surface. In particular, we take a Fermi surface appropriate for cuprates that can be deduced from the tight-binding model dispersion for a square lattice:

$$\xi(\mathbf{k}) = -2t_0(\cos k_x + \cos k_y) - 4t_0' \cos k_x \cos k_y - 2t_0''(\cos 2k_x + \cos 2k_y) - \mu, \tag{14}$$

and a d-wave superconducting gap on the square lattice,

$$\Delta(\mathbf{k}) = \Delta(T)(\cos k_x - \cos k_y). \tag{15}$$

We use the parameters appropriate for BSCCO [66]: $t_0 = 126\,\text{meV}$, $t_0' = -36\,\text{meV}$, $t_0'' = 15\,\text{meV}$, $\mu = -135\,\text{meV}$, and we take $k_B T_c = 9\,\text{meV}$. Note that the unit cell of BSCCO contains two CuO_2 layers. The resulting twisted double bilayer structure does not alter qualitatively any of the results, as is shown in Appendix A; here we focus on the single-layer unit cell for clarity of presentation. In this subsection, we keep the tunneling momentum-independent but generalize this below. For numerical calculation in this and the next section, we additionally rotated the momenta by $-\theta_0/2$ in both layers.

In Fig. 4 we show the twist angle and temperature dependence of $I_c^{(2)}(\theta_0, T)$. One observes a very pronounced deviation from the $\cos 2\theta_0$ form. In particular, the steep initial decrease of $I_c^{(2)}(\theta_0, T \ll T_c)$ with θ_0 resembles the results of experiments on whisker twist junctions [52]. We note that unlike Ref. [59], the deviation from the $\cos 2\theta_0$ form appears already in the lowest-order tunneling approximation, consistent with previous works [55]. Another feature that is present in our results is a broad maximum in I_c at around $\theta_0 = 20°$. As shown in the inset of Fig. 4(a), close to this twist angle, the Fermi surfaces of the two layers start crossing each other near the Brillouin zone boundary. The contribution of this region to Eq. (6) is positive and is maximized when the Fermi surfaces cross [i.e., $\xi(\mathbf{k}) = \xi(\tilde{\mathbf{k}}) = 0$], suggesting that the maximum reflects the appearance of this crossing. A more detailed discussion of this point is presented in Sec. III C.

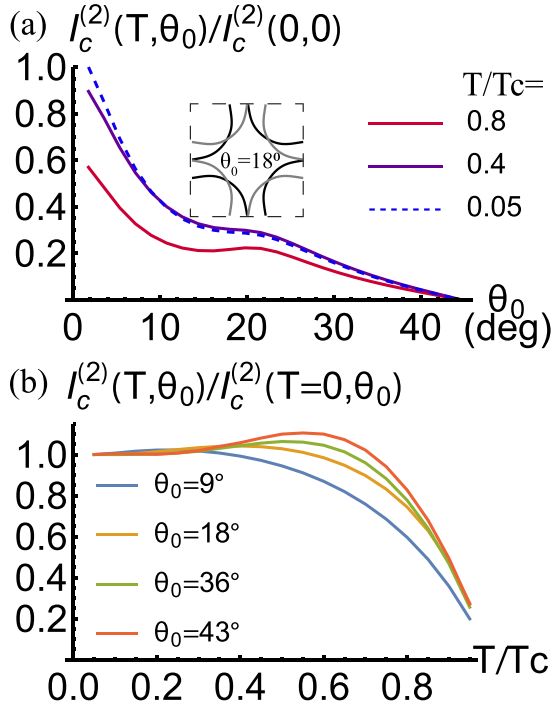

FIG. 4. Second-order approximation of the critical current $I_c^{(2)}(T,\theta_0)$ in Eq. (6) for a cupratelike Fermi surface with parameters from BSCCO. (a) Twist angle (θ_0) dependence of $I_c^{(2)}$ for various temperatures (T) displaying a local maximum near $\theta_0 \approx 20^\circ$. The inset shows an overlay of two twisted cupratelike Fermi surfaces at $\theta_0 = 18^\circ$ corresponding to a broad maximum in $I_c^{(2)}$ at low temperatures. (b) Nonmonotonic temperature dependence of $I_c^{(2)}$, which becomes more pronounced near $\theta_0 = 45^\circ$. See Appendix A for how these conclusions also apply to twisted double bilayers as appropriate for BSCCO.

Moreover, we find a nonmonotonic temperature dependence of I_c [Fig. 4(b)] that becomes relatively more pronounced towards $\theta_0 = 45^\circ$ (we note, however, that sufficiently close to $\theta_0 = 45^\circ$, the higher-order terms in t will become dominant). The nonmonotonicity in this case appears stronger than for the circular Fermi surface case.

1. Momentum-dependent tunneling

Finally, we address the effects of the momentum dependence of the tunneling. This is indeed relevant for cuprates, where the dominant tunneling between the $d_{x^2-y^2}$-like orbitals occurs via intermediate s-like orbitals [67], leading to $t(\mathbf{k}) \approx t_z(\cos k_x - \cos k_y)^2$ in the bulk of the material. At a twisted interface, $d_{x^2-y^2}$-like orbitals in the twisted layer are rotated, leading to

$$t(\mathbf{k}) = t_z(\cos k_x - \cos k_y)(\cos \tilde{k}_x - \cos \tilde{k}_y). \tag{16}$$

In Fig. 5 we present the $I_c^{(2)}(\theta_0, T)$ computed with the momentum-dependent tunneling (16). Remarkably, the temperature dependence of $I_c^{(2)}$ is always monotonic in this case, while the twist angle dependence is quite similar to the case of a momentum-independent tunneling. Thus, we see that the temperature and twist angle dependence of the critical current for a twist junction depends strongly on the Fermi surface geometry and the form of the tunneling in the coherent

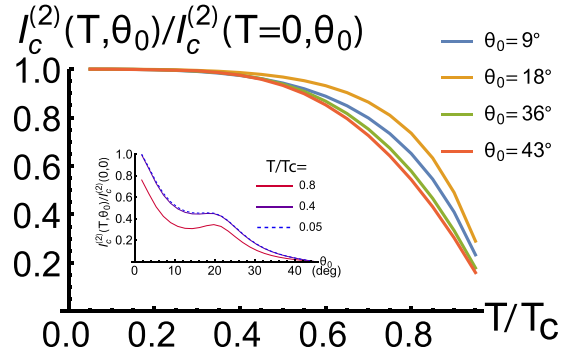

FIG. 5. Second-order approximation of the critical current $I_c^{(2)}(T,\theta_0)$ in Eq. (6) incorporating the momentum-dependent tunneling relevant for BSCCO in Eq. (16). As in Fig. 4 we are also taking a cupratelike Fermi surface with parameters from BSCCO. The temperature dependence of the normalized $I_c^{(2)}$ no longer displays the maximum found in Fig. 4(b). The inset shows the twist angle dependence of $I_c^{(2)}$ that remains qualitatively similar to Fig. 4(a).

(momentum-conserving) tunneling limit. We note that strong deviations from $I_c(\theta_0)$ going like $\sim \cos 2\theta_0$ are observed for all models considered, which is in contrast to the recent experiments on cryogenically prepared twist junctions [48–50]. We also find similar conclusions for a more realistic description of BSCCO that uses the appropriate bilayer unit cell as described in Appendix A. As we show in Sec. IV below, in the presence of weak momentum relaxing effects at the twist junction, the $\cos 2\theta_0$ dependence appears clearly.

C. Qualitative assessment of $I_c(\theta_0, T)$: Nodal/antinodal dichotomy

We now present qualitative arguments allowing additional insight into the results of the previous sections. Let us start with the nonmonotonic temperature dependence of Secs. III A and III B. As the gap amplitude, per Eq. (8), is a strictly monotonic function of temperature, one expects that if the summand in Eq. (6) was positive for all $\mathbf{k}$, the resulting $I_c(T)$ would be monotonic. This is not the case, however, at a finite twist angle. In particular, in between two nodal lines of the superconducting gap, which were aligned at $\theta_0 = 0$, the order parameter has a different sign for two layers, leading to a negative contribution to Eq. (6).

This is especially clear in the case of a cupratelike Fermi surface at a finite twist angle, which is displayed in Fig. 6. As has been noted above, the contribution to Eq. (6) is enhanced near the points where Fermi surfaces cross. At low twist angle, such a crossing occurs in the near-nodal (N) region, where the order parameter has opposite signs for two layers. For larger twist angles, an additional crossing appears in the antinodal (AN) region (close to the Brillouin zone boundary). There, on the contrary, the order parameters of the two layers have the same sign. The contributions of these regions to I_c read

$$\delta I_c^{N}(T) \sim -\frac{\Delta_N(\theta_0, T)\tanh\frac{\Delta_N(\theta_0,T)}{2T}}{\left|\mathbf{v}_F^{1,N} \times \mathbf{v}_F^{2,N}\right|},$$
$$\delta I_c^{AN}(T) \sim \frac{\Delta_{AN}(\theta_0, T)\tanh\frac{\Delta_{AN}(\theta_0,T)}{2T}}{\left|\mathbf{v}_F^{1,AN} \times \mathbf{v}_F^{2,AN}\right|}, \tag{17}$$

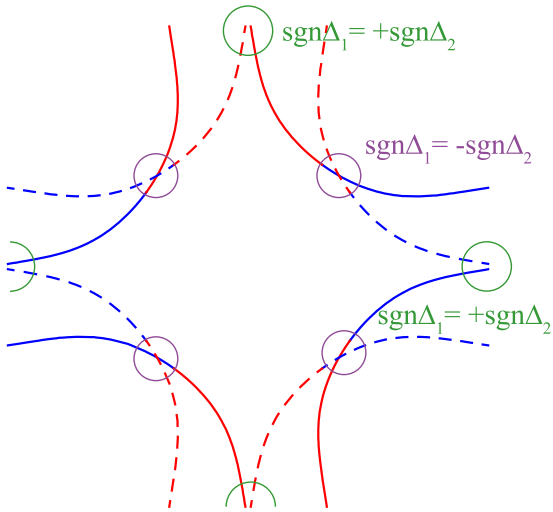

FIG. 6. Twisted cupratelike Fermi surfaces. Fermi surface schematic for $\theta_0 = 18^\circ$ with the order parameter sign shown by color. Solid (dashed) lines correspond to the Fermi surface of the top (bottom) layer. In the nodal region (purple circle), the order parameters of the two layers have opposite signs due to twist. This leads to a negative contribution to the critical current, Eq. (17). In contrast, in the antinodal region (green circles), the order parameter has the same sign for both layers.

where $\mathbf{v}_F^{(1,2),(N,AN)}$ are the Fermi velocities at the points where the Fermi surfaces cross, and $\Delta_{N,AN}$ are the gaps in the N and AN regions. At low twist angles, only the negative nodal contribution is relevant (there are, of course, also contributions away from the crossing, which lead to the overall critical current being positive). It becomes larger in magnitude on cooling, providing an explanation for the decreasing I_c. Its magnitude is suppressed at low twist angles due to the smallness of the gap at the Fermi surface crossing $\Delta_N(\theta_0, T) \sim \theta_0$. This explains why the nonmonotonicity is enhanced by twist. We note that a similar coexistence of negative and positive contributions to the critical current from different regions in momentum space was observed for in-plane d/d junctions [64].

At larger twist angles, the antinodal crossing appears, which contributes an enhanced positive correction to I_c. This is indeed what is seen to occur in Fig. 4(a). At low temperatures, both nodal and antinodal contributions saturate to finite values. However, $\Delta_{AN}(T)/\Delta_N(T) \sim \text{const} > 1$; consequently, for temperatures $2\Delta_N(0) < T < 2\Delta_{AN}(T = 0)$, the tanh in $\delta I_c^{AN}(T)$ is already saturated to a constant, while the tanh in $\delta I_c^{N}(T)$ will continue to grow in absolute magnitude on cooling. Thus for temperatures $2\Delta_N(0) < T < 2\Delta_{AN}(0)$, the total $\delta I_c^{AN}(T) + \delta I_c^{N}(T)$ will decrease on cooling, implying a nonmonotonic $I_c(T)$.

Finally, the effect of the momentum-dependent tunneling on the temperature dependence of I_c can be understood from this picture. Indeed, the tunneling Eq. (16) is very strongly suppressed in the nodal region, vanishing as θ_0^2 for low twist angles. This suppresses the contribution of the nodal region to I_c in agreement with it being the source of nonmonotonicity.

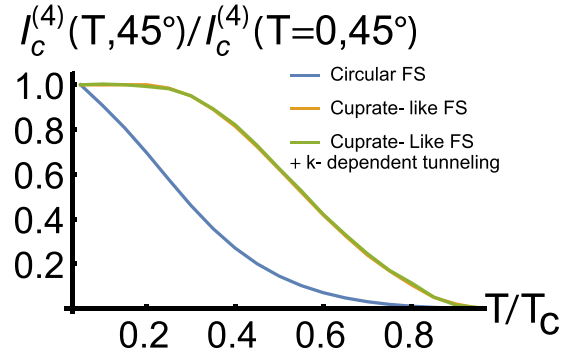

FIG. 7. The fourth-order contribution to the critical current at $\theta_0 = 45^\circ$. Temperature dependence of the cotunneling critical current, Eq. (7), for three models with coherent tunneling: circular FS (blue), cupratelike FS (yellow), and cupratelike FS with momentum-dependent tunneling (green); the latter two are almost identical.

D. $I_c(T)$ at $\theta_0 = 45^\circ$ due to cotunneling

As has been shown above (see, e.g., Fig. 3), the second-order tunneling in Eq. (6) dominates the Josephson effect apart from in the vicinity of $\theta_0 = 45^\circ$, where the cotunneling of Cooper pairs in Eq. (7) takes over. We now consider the temperature dependence of the cotunneling critical current.

In Fig. 7 we present the temperature dependence of the cotunneling critical current for the three models considered above. In all of the cases, the dependence is steeper than for the tunneling critical current [see Figs. 2(b), 4(b), and 5]. On approach to T_c, the cotunneling critical current is suppressed much stronger than the tunneling one, as is expected from the general expression in Eq. (7). This distinct temperature dependence may serve as a qualitative indicator of the presence of a second harmonic in the CPR.

IV. EFFECTS OF INTERFACE INHOMOGENEITY ON $I_c(\theta_0, T)$

Here we study the consequences of the broken translational symmetry at the interface due to lattice supermodulations, moiré quasiperiodicity, atomic scale interface roughness, or disorder, all of which result in the in-plane momentum not being conserved during tunneling $t(\mathbf{k}, \mathbf{k}' \neq \mathbf{k}) \neq 0$. We will work in the weak tunneling approximation here, using the expansion in Eqs. (6) and (7). Several models for $t(\mathbf{k}, \mathbf{k}')$ can be considered. First, for a purely incoherent tunneling $t(\mathbf{k}, \mathbf{k}') = t_0$, corresponding to atomic-scale disorder, such as in the case of the Ambegaokar-Baratoff formula for s-wave superconductors [68,69], Eqs. (6) and (7) yield *identically zero* due to the d-wave symmetry of the order parameters. For a superposition of fully coherent and incoherent terms, $t(\mathbf{k}, \mathbf{k}') = t_0 + t_1\delta_{\mathbf{k},\mathbf{k}'}$, it is evident that only t_1 will contribute in the lowest order in Eq. (6). In the recent experiments [48–50,60], the critical current at the interfaces prepared at $\theta_0 = 0$ was observed to be similar to the one expected between individual layers in the bulk. That rules out the presence of strong atomic-scale disorder at the twist interface.

For the more realistic case of weak nanoscale disorder (such as structural supermodulations [70]), with a lengthscale

significantly larger than the unit cell size, the tunneling has a characteristic momentum spread that is smaller than the size of the Brillouin zone. We consider the case in which tunneling is not exactly momentum-conserving, modeled with a spread of σ in typical momentum differences $|\mathbf{k}-\mathbf{k}'|$. This can be implemented by replacing $|t(\mathbf{k},\mathbf{k}')|^2$ with a function with a width σ (e.g., a Gaussian) denoted $|t_\sigma(\mathbf{k},\mathbf{k}')|^2$ [54,55]. We choose the normalization such that in the limit $\sigma \to 0$ we recover coherent tunneling, i.e., $|t(\mathbf{k},\mathbf{k}')|^2 = t_0^2\delta(\mathbf{k}-\mathbf{k}')$, i.e.,

$$|t_\sigma(\mathbf{k},\mathbf{k}')|^2 = \frac{t_0^2}{2\pi\sigma^2} e^{-\frac{|\mathbf{k}-\mathbf{k}'|^2}{2\sigma^2}}. \tag{18}$$

For momenta close to the Fermi surface, one can further split the constraint on the tunneling momentum into those on the momentum magnitude and the polar angle in Eq. (10):

$$\begin{aligned}|\mathbf{k}-\mathbf{k}'|^2 &= (k-k')^2 + 4kk'\sin^2\frac{\theta-\theta'}{2}\\ &\approx (k-k')^2 + k_F^2(\theta-\theta')^2,\end{aligned} \tag{19}$$

where $\theta^{(\prime)} + 2\pi \equiv \theta^{(\prime)}$. It follows then that the angular spread of the tunneling is equal to $\tilde{\sigma} = \sigma/k_F$.

Before we proceed with concrete calculations, it is useful to estimate the expected magnitudes. For $k_F \gg \sigma \gg \Delta/v_F$, the second-order current in Eq. (6) is proportional to $\frac{t^2}{\sigma^4}\frac{\sigma}{k_F}\Delta(\frac{k_F}{\hbar v_F})^2$, where the second factor arises from limiting the angle deviation between $\mathbf{k}$ and $\mathbf{k}'$ to $\frac{\sigma}{k_F}$, and the last one is just the density of states from two k-integrals. Proceeding in a similar way for the second-harmonic part of (7), it is proportional to $\frac{t^4}{\sigma^8}(\frac{\sigma}{k_F})^3\Delta(\frac{k_F}{\hbar v_F})^4$. Thus the ratio scales as $I_c^4(\theta=45^\circ)/I_c^2(\theta=0) \sim \frac{t^2}{(\hbar v_F\sigma)^2}$. For coherent (momentum-conserving) tunneling, the estimate is $[I_c^4(\theta=45^\circ)/I_c^2(\theta=0)]_{\rm coh} \sim t^2/(\Delta E_F)$ [71]. Given that $E_F \gg \Delta$ is expected to be by far the largest scale in the problem, inhomogeneity can in principle increase the tunneling strength at 45° relative to $\theta = 0$. We note, however, that our model of inhomogeneity effects differs from that in [72], in that in our case the twist angle remains well-defined and we do not find the formation of 0 and π regions in real space.

A. Second-order tunneling $I^{(2)}$

First, we consider the second-order tunneling process with interfacial disorder at the twist junction. The angular integrals of $\mathbf{k},\mathbf{k}'$ in Eq. (6) are performed in Appendix B. To make further progress analytically, we take $\xi(\mathbf{k}) = \xi(k)$ and $\Delta(\mathbf{k}) = \Delta(T)\cos 2\theta$ as in Sec. II B and decompose the angular part of the integrand into a Fourier series utilizing Eq. (19). This allows for the Fourier series to act as a controlled expansion, since the contributions from higher-order terms in the series are being suppressed by powers of $e^{-2\tilde{\sigma}^2m^2}$ at Fourier order m and $\tilde{\sigma} = \sigma/k_F$; see Eq. (B2).

For the integral over the magnitude of $\mathbf{k},\mathbf{k}'$ (i.e., k,k') in Eq. (6), we consider two limiting cases. For smooth inhomogeneity (SI) we assume $\hbar v_F\sigma \ll \sqrt{\Delta^2(T)+(\pi T)^2}$, which can be valid at all T. This limit corresponds to the inhomogeneity lengthscale being longer than the BCS coherence length of the superconductor. We can then take the limit $\sigma \to 0$ in the k,k' integral [but not in the integrals over angle θ,θ'; see Eqs. (B1) and (B5)] to obtain

$$\begin{aligned}I_{\rm SI}^{(2)}(\varphi,T,\theta_0) \approx \mathcal{A}t_0^2 e^{-2\tilde{\sigma}^2}\big[&i_1^{(2)}(T)\cos(2\theta_0)\\ &+ i_3(T)\cos(6\theta_0)e^{-16\tilde{\sigma}^2}\big]\sin\varphi,\end{aligned} \tag{20}$$

where for simplicity of presentation we have defined the constant $\mathcal{A} = \frac{ek_F}{4\pi^3\hbar^2 v_F}$, and we introduced the contributions to the first $i_1^{(2)}(T)$ and third harmonics $i_3^{(2)}(T)$ of the Fourier expansion that are evaluated in Appendix B. In the limiting cases of $T \approx 0$ and T_c, we obtain

$$i_1^{(2)}(T) \approx \begin{cases} 2(\log 4 - 1), & T \to 0,\\ 0.1\frac{\Delta^2(T)}{T_c^2}, & T \to T_c,\end{cases} \tag{21}$$

as well as

$$i_3^{(2)}(T) \approx \begin{cases} 2(\log 4 - 4/3), & T \to 0,\\ 4\times 10^{-5}\frac{\Delta^6(T)}{T_c^6}, & T \to T_c.\end{cases} \tag{22}$$

Note that $I_c(0)$ is then independent of $\Delta(T)$. This suggests that the qualitative signature of this regime is the independence of $I_c(T=0)$ of T_c, the latter being controlled by, e.g., doping. The resulting dependence of the critical current on the twist angle is consistent with the form $I_c(\theta_0) \sim \cos(2\theta_0)$ as observed in experiments on BSCCO twist junctions [48–50].

In the opposite limit of rough inhomogeneity (RI), $\hbar v_F\sigma \gg \sqrt{\Delta^2(T)+(\pi T)^2}$, we get the more usual Ambegaokar-Baratoff [69] -like expression (see Appendix B)

$$\begin{aligned}I_{\rm RI}^{(2)}(\varphi,T,\theta_0) \approx \frac{\mathcal{A}t_0^2 e^{-2\tilde{\sigma}^2}}{\sqrt{2\pi}\hbar v_F\sigma} \times \big(&\tilde{i}_1^{(2)}(T)\cos(2\theta_0)\\ &+ \tilde{i}_3^{(2)}(T)\cos(6\theta_0)e^{-16\tilde{\sigma}^2}\big)\sin\varphi,\end{aligned} \tag{23}$$

where the first harmonic is now

$$\tilde{i}_1^{(2)}(T) \approx \begin{cases} 6.035\Delta(T), & T \to 0,\\ \frac{\pi^2}{4}\frac{\Delta^2(T)}{T_c}, & T \to T_c,\end{cases} \tag{24}$$

and the third harmonic is given by

$$\tilde{i}_3^{(2)}(T) \approx \begin{cases} 0.18\Delta(T), & T \to 0,\\ 3\times 10^{-4}\frac{\Delta^2(T)}{T_c}, & T \to T_c.\end{cases} \tag{25}$$

Again, we use the constant $\mathcal{A} = \frac{ek_F}{4\pi^3\hbar^2 v_F}$, and we have introduced distinct contributions to the first $\tilde{i}_1^{(2)}(T)$ and third harmonics $\tilde{i}_3^{(2)}(T)$ of the Fourier expansion in the limit of rough inhomogeneity at the twist interface. Note that the distinction "rough" does not imply a strong disorder at the interface, but rather characterizes the lengthscale of the typical inhomogeneities.

Let us now consider the temperature dependence of the lowest-order critical current following the $\cos(2\theta_0)$ twist angle dependence. In Fig. 8(a) we present the temperature dependence of the lowest twist-angle harmonic of the critical current deduced from (20) and (23) and taking the temperature dependence of the gap from the numerical solution of Eq. (13). Importantly, in both cases it appears monotonic. These results suggest that at the level of weak tunneling, the nonmonotonic temperature dependence of I_c is intimately related to coherence of the tunneling.

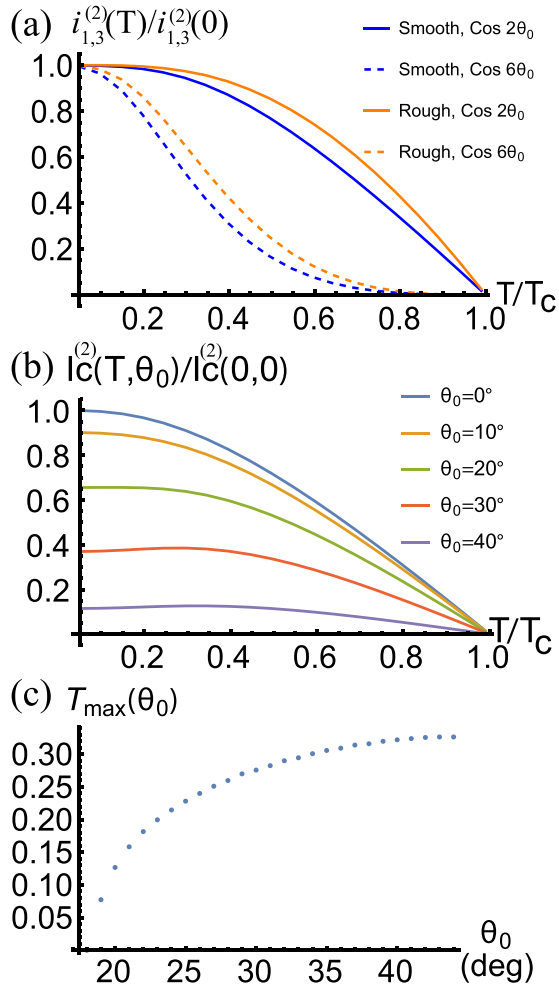

FIG. 8. Effects of weak interfacial inhomogeneities. (a) Temperature dependence of the normalized tunneling critical current harmonics normalized to their values at $T = 0$ for smooth $[i_1^{(2)}(T)/i_1^{(2)}(0), i_3^{(2)}(T)/i_3^{(2)}(0)$ in (20)] (blue, "smooth") and rough $[i_1^{(2)'}(T)/i_1^{(2)'}(0), i_3^{(2)'}(T)/i_3^{(2)'}(0)$ in (23)] (yellow, "rough") interface inhomogeneity compared to the superconducting coherence length. (b) Temperature dependence of the second-order critical current $I_c^{(2)}(T, \theta_0)$ (normalized to its $T = 0, \theta_0 = 0$ value) for several values of the twist angle with two harmonics included in the smooth interface limit (20) with $\tilde{\sigma} = 0.15$. (c) Temperature $T_{\max}(\theta_0)$ of the critical current maximum in (b).

In both cases of smooth and rough inhomogeneity, the $\cos(6\theta_0)$ contribution appears to be strongly suppressed numerically (in addition to the exponential suppression due to angular spread) by almost an order of magnitude at low T and by several orders of magnitude close to T_c. The $\cos(6\theta_0)$ contribution has the same sign as the $\cos(2\theta_0)$ one in both the clean and rough limit. However, the relative sign of the two contributions changes with θ_0 well before $\theta_0 = 45°$. In the clean limit, this leads to a clear nonmonotonic temperature dependence of I_c [Fig. 8(b)], which shows a maximum at a finite temperature $T_{\max}$ for $\theta_0 > 18°$ [Fig. 8(c)], close to the values observed in experiment [48].

To conclude this subsection, we have found that relaxing momentum conservation at the twist interface naturally accounts for the observation of

$$I_c(\theta_0, T) \sim \cos(2\theta_0) \tag{26}$$

at low temperatures seen in recent experiments [48–50]. The high value of the critical current of the twist junction observed in experiment [48] also indicates that the momentum relaxation arises from nanoscale inhomogeneities, such as the ones that arise from structural supermodulation [70] and not atomic-scale disorder. This is consistent with the atomically sharp interfaces with structural supermodulations observed using transmission electron microscopy in Ref. [48].

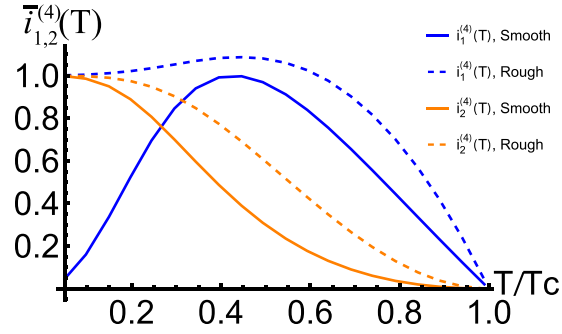

FIG. 9. The fourth-order contribution to the critical current with weak interfacial inhomogeneities. Temperature dependence of the normalized fourth-order critical current harmonics $i^{(4)}_{1,2}(T)$, Eq. (28). $i_1^{(4)}(T)$ in the weak roughness limit is normalized to its maximal value, while the rest are normalized to their values at $T = 0$.

B. Fourth-order tunneling $I^{(4)}$

Finally, we discuss the fourth-order tunneling contribution to the critical current. Applying the same expansion in twist angle harmonics to Eq. (7), we obtain the following result for the two leading harmonics with a common form to both the SI and RI regimes:

$$I^{(4)} = I^{(4)}_{1,c}(T)\cos 2\theta_0 \sin\varphi + I^{(4)}_{2,c}(T, \theta_0)\sin 2\varphi, \tag{27}$$

where the coefficients of the first harmonic $I^{(4)}_{1,c}(T)$ and second harmonic $I^{(4)}_{2,c}(T, \theta_0)$ of the CPR are given by

$$I^{(4)}_{1,c}(T) = -\frac{et_0^4 k_F \sigma^2 e^{-3\tilde{\sigma}^2}}{\hbar^2 v_F (2\pi)^6} i_1^{(4)}(T),$$
$$I^{(4)}_{2,c}(T, \theta_0) = -\frac{et_0^4 k_F \sigma^2 e^{-4\tilde{\sigma}^2}}{\hbar^2 v_F (2\pi)^7}\left(\cos 4\theta_0 + 2e^{-4\tilde{\sigma}^2}\right) i_2^{(4)}(T) \tag{28}$$

and the expressions for $i_1^{(4)}(T)$ and $i_2^{(4)}(T)$ are given in Appendix B in both the SI and RI regimes; their temperature dependence is shown in Fig. 9. We find that in the limit of SI, $i_1^{(4)}$ is strongly suppressed at low temperatures in contrast to $i_2^{(4)}$, which saturates to a nonzero value. In contrast, in the opposing limit of a RI we find both contributions survive to low temperatures.

Several qualitative conclusions can be drawn from (27). First, the suppression of this term with roughness is much stronger than for the usual tunneling term due to the additional factors of $\sigma^2 e^{-\tilde{\sigma}^2}$. Additionally, the twist angle dependence of

the second harmonic CPR ($\sim \sin 2\varphi$) term is modified due to disorder via the term $\cos 4\theta_0 + 2e^{-4\tilde{\sigma}^2}$ in Eq. (28). This is remarkable because the formally higher harmonic in the angular dependence ($\cos 4\theta_0$) appears more resilient to the inhomogeneity that effectively averages over the angle. Qualitatively, the two contributions arise from the two contributions present in Eq. (7), $\Delta(\mathbf{k}_2)\Delta(\mathbf{k}_4) \propto \cos 2(\theta_2 - \theta_4) + \cos 2(\theta_2 + \theta_4 + 2\theta_0)$, which can be attributed to a cotunneling of two Cooper pairs in and out of phase (within one layer). Since θ_4 and θ_2 are not directly constrained to be close with a direct tunneling matrix element (only indirectly via θ_3, θ_4), they can deviate from one another stronger than the angles between two layers (e.g., θ_1 and θ_3), and thus the $\cos 2(\theta_2 - \theta_4)$ factor leads to a stronger suppression in the presence of inhomogeneity.

This implies profound consequences for the system close to $\theta_0 = 45^\circ$: if the disorder strength is sufficiently large, it is possible to destroy the topological superconducting phase at $\theta_0 = 45^\circ$ because the $\cos 4\theta_0$ will then be dominant and negative, which will change the overall sign of the second harmonic in the CPR. In that case, the state with a dominant second harmonic in the CPR would still have a free-energy minimum at $\varphi = 0$ [45,46], indicating the absence of a spontaneous time-reversal symmetry breaking and the topological phase. For the Gaussian momentum smearing used here in Eq. (18), we find that a topological to trivial superconductor transition occurs at a critical value of the disorder strength $\tilde{\sigma}_c \approx 0.42$, which corresponds to an angular spread of around $\pm 24^\circ$ [see Eq. (18)] for incoherent tunneling. Importantly, such a broad interlayer momentum-dependent tunneling is inconsistent with the atomically sharp interface observed experimentally [48]. In summary, for a twist $\theta = 45^\circ$ and $\tilde{\sigma} < \tilde{\sigma}_c$, the ground state is a topological superconductor that breaks time-reversal symmetry, whereas for $\tilde{\sigma} > \tilde{\sigma}_c$ the superconductor is trivial and the time-reversal symmetry is restored by inhomogeneity.

V. EXPERIMENTAL PROBES OF THE CURRENT-PHASE RELATION NEAR $\theta_0 = 45^\circ$

In the previous sections, we have discussed the qualitative features of the dependence of the critical current in twisted d-wave superconducting interfaces on the twist angle and temperature. We have established that many peculiar effects can be attributed to the lowest-order tunneling in Eq. (6). However, near $\theta_0 = 45^\circ$, the higher-order processes in Eq. (7) of Cooper pair cotunneling start to dominate, changing the CPR to include the second $\sin(2\varphi)$ harmonic. Here, we discuss how the CPR can be measured experimentally near $\theta_0 = 45^\circ$. First, we will address the behavior of the twist junctions in a magnetic field, which results in a coordinate dependence of the phase difference across the interface $\varphi \to \varphi(x)$. We will consider two distinct device geometries in Fig. 10, where the setup in Fig. 10(a) is consistent with the experimental layout of Ref. [48]. Second, we will study the effect of a microwave drive (in the absence of a static magnetic field), which induces Shapiro steps due to the phase difference across the twist junction becoming time-dependent, $\varphi \to \varphi(\tau)$. Both of these setups, as will be shown, allow us to reveal the contribution of the cotunneling-induced second harmonic in the CPR.

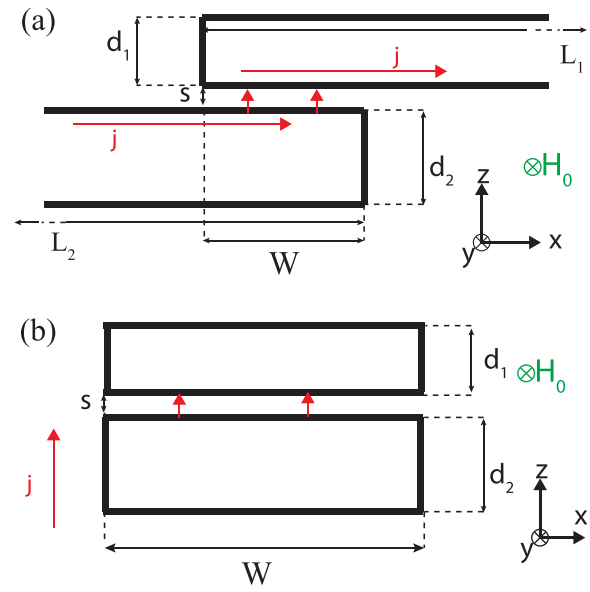

FIG. 10. The two junction geometries considered. The in-line geometry is shown in (a) [73] and the vertical geometry in (b). The current (red arrows) is injected along the x-axes in geometry (a) and along the z-axes in geometry (b). In both cases, the magnetic field is applied along the y axis; the length of the junctions along y is denoted D.

We begin by discussing the characteristic lengthscales relevant for a twist junction. Generally, the characteristic variation of φ along the length of the junction is given by the Josephson length [74]

$$\lambda_J \sim 1/\sqrt{j_c}, \tag{29}$$

where j_c is the critical current density. Near $\theta_0 = 45^\circ$, as discussed above in Secs. III and IV, the CPR contains two sinusoidal harmonics: $\sin\varphi$ and $\sin 2\varphi$, e.g., see Eqs. (20) and (27). The first harmonic corresponds to the tunneling of Cooper pairs that is required to vanish at 45° due to the d-wave nature of the superconductors, while the second harmonic describes a higher-order process: cotunneling of Cooper pairs. Correspondingly, we introduce two Josephson lengths $\lambda_{J1}(\theta_0, T) \sim 1/\sqrt{|j_c^1(\theta_0, T)|}$ and $\lambda_{J2}(\theta_0, T) \sim 1/\sqrt{|j_c^2(\theta_0, T)|}$ (the quantitative definitions will be given below).

Denoting W as the relevant linear junction size (e.g., width in the direction perpendicular to the applied field), we find three qualitative regimes, each dominated by the shortest length scale. We assume $j_c^2 \ll j_c^1(\theta = 0)$ due to the smallness of the interlayer tunneling at the interface and $\lambda_{J1}(\theta_0 = 0, T = 0) < W$. Given the result in Secs. III and IV, one can then identify the position of these regimes in the T-θ_0 phase diagram, as shown in Fig. 11.

Before we move on to the magnetic field effects, it is important to remark that the device geometry may affect the I_c measurements in the regime III even without the external field. For example, let us consider the two device geometries depicted in Fig. 10. For the vertical geometry in Fig. 10(b), the critical current is given by $j_c DW$; however, for an in-line geometry shown in Fig. 10(a), the critical current would be equal

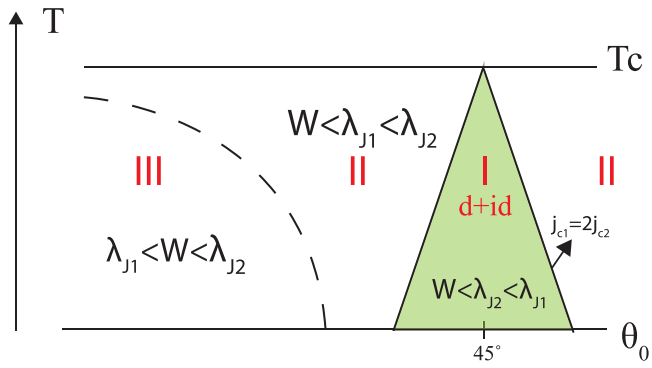

FIG. 11. Qualitative phase diagram and the corresponding Josephson length λ_J regimes for the twist junction. The smallest lengthscale determines the character of spatial variations of the supercurrent across the junction: in regime *III* the current is confined to within λ_{J1} of the junction edges [73,74], while in *I*, *II* the current is evenly distributed along the junction length. In regimes *III*, *II* the first harmonic of the CPR dominates whereas region *I* is controlled by the second harmonic in the CPR. The boundary between *II* and *I* occurs at the time-reversal symmetry breaking transition into the topological $d + id$ superconducting phase [46,47].

to $4D\lambda_J j_c \sim \sqrt{j_c}$ [73,75]. In the latter case, the critical current is independent of the junction width W and flows mostly along the junctions edges. In this case, the experimentally observed temperature and twist angle dependence of the critical current has to be compared with $\sqrt{I_c}$ from Secs. III and IV rather than with I_c. In contrast to the above, in regimes *I* and *II*, where $\lambda_{J1,2} \gg W$, the critical current will always be given by $j_c DW$, independent of the device geometry [73,74]. In the previous experiments [76] on intrinsic BSCCO junctions ($\theta_0 = 0$), the crossover to the width-independent regime occurred at $W \approx 20$ μm.

A. Twist junctions in a parallel magnetic field

We consider the Josephson effect at the interface between two flakes of length L_1 and L_2 and thicknesses d_1 and d_2 with an overlap of length W as depicted in Fig. 10. We take both flakes as well as the overlap region to be of rectangular shape for simplicity; while the deviations from the rectangular cross-section can affect the critical current oscillations in a magnetic field [74], they do so mostly for fields larger than the first Fraunhofer pattern zero, and thus they are not our main focus here.

The discrete layered structure of cuprates can play an important role for magnetic field effects [77]. The relevant lengthscale for the field variation between layers is [77] $s\frac{\lambda_c}{\lambda_{ab}} \lesssim$ μm (where $s \approx 1.5$ nm is the interlayer spacing and $\frac{\lambda_c}{\lambda_{ab}} \lesssim 10^3$ [76,78] is the ratio of the penetration depths along the c axes and ab plane); the overlap regions in the experiments are generally longer than that ($W \sim 10$ μm) resulting in a length-independent characteristic field [79] $H_0^{FG} = \frac{\Phi_0}{\pi^2 s^2 \lambda_c/\lambda_{ab}} \gtrsim 0.1$ T [76]. The characteristic fields observed for the Fraunhofer patterns near $\theta_0 = 45^\circ$ in recent experiments [48] are less than 100 G (0.01 T), implying that the layered structure of the flakes is not important. However, even at the lowest fields, vortices may enter the flakes (the H_{c1} values in cuprates are quite low [78]), creating additional phase distortions at the junction. Note that the flakes used in the experiments [48] are typically thinner than $\lambda_{ab} \sim 0.2$ μm [78,80] by a factor of order 2–4, which can result in a somewhat enlarged H_{c1}. In the derivation below, we will ignore the presence of vortices in flakes in proximity to the junction, corresponding to sufficiently low fields, i.e., $H_0 \lesssim H_{\rm vort} \sim \frac{\Phi_0}{W d_{1,2}}$ (i.e., there is less than one vortex in the flakes in proximity to the junction). For typical $W \sim 10$ μm and $d \sim 0.05 - 0.1$ μm, $H_{\rm vort}$ is between 20 and 40 G.

Consequently, limiting our considerations to sufficiently low fields to ignore the layered structure of the flakes and vortices, we can use the London equations inside the flakes to describe the screening of the magnetic field by the superconducting flakes. Note that at the interface between the two flakes (the twist junction), the continuum approximation cannot be used, as the phase difference can be large across the interface; this will be taken into account below.

Inside a single rectangular flake of size $d \times L$, taking the coordinate origin in its center, the London equations of the magnetic field $H(x, z)$ take the form

$$\begin{aligned} &\lambda_c^2 \frac{\partial^2 H}{\partial x^2} + \lambda_{ab}^2 \frac{\partial^2 H}{\partial z^2} = H, \\ &H|_{z=+(-)d/2} = H_0, \quad H|_{x=\pm L/2} = H_0, \\ &H|_{z=-(+)d/2} = H_0 + H_j(x), \end{aligned} \tag{30}$$

where $H_j(x)$ is the magnetic field inside the twist junction. The signs for the boundary condition along z are for the case when the junction is at the bottom (top) of the flake.

The bulk of the flakes produces a Meissner effect in magnetic field, generating screening currents that flow through the junction affecting the phase difference across it,

$$\frac{\partial H}{\partial z} = -\frac{4\pi}{c} j_x = \frac{\Phi_0}{2\pi\lambda_{ab}^2}\left[\frac{\partial \Phi}{\partial x}(x, z) + \frac{2\pi}{\Phi_0} A_x(x, z)\right], \tag{31}$$

where Φ is the phase of the superconducting order parameter. Subtracting these equations at the top and the bottom of the interface (and assuming the interface thickness s to be much smaller than the field variation lengthscale),

$$\left.\frac{\partial H}{\partial z}\right|_{\rm top}(x) - \left.\frac{\partial H}{\partial z}\right|_{\rm bottom}(x) = \frac{\Phi_0}{2\pi\lambda_{ab}^2}\left[\frac{\partial \varphi}{\partial x}(x) + \frac{2\pi s}{\Phi_0} H(x)\right], \tag{32}$$

where $\varphi(x) = \Phi_{\rm top}(x) - \Phi_{\rm bottom}(x) + \frac{2\pi s}{\Phi_0} A_z(x, z)$ is the gauge-invariant phase difference across the junction, and $\Phi_0 = \pi\hbar c/|e|$ is the flux quantum.

1. *Fraunhofer patterns close to $\theta_0 = 45^\circ$*

For a weak junction, we can ignore the fields generated by the Josephson current, such that $H_j(x) = 0$ in Eq. (30).

For $L \gg \lambda_c$, the solution away from the edges $L/2 - |x| \gg \lambda_c$ can be taken as x-independent and has the form

$$H_{L\to\infty}(z) = H_0 \frac{\cosh\frac{z}{\lambda_{ab}}}{\cosh\frac{d}{2\lambda_{ab}}}. \tag{33}$$

For the full problem in Eq. (30), we use the variable-separation ansatz as described in Appendix C.

Using the expression for $H(x,z)$ given in Appendix C, one can evaluate $\varphi(x)$ directly using Eq. (32) [note that the flakes in the in-line geometry, Fig. 10(a), are shifted along x]:

$$-\varphi(x) = C + \frac{2\pi H_0 s x}{\Phi_0} - \int_0^x dx' 2\pi\lambda_{ab}^2 \left(\frac{\partial H}{\partial z}\bigg|_{\text{top}}(x') - \frac{\partial H}{\partial z}\bigg|_{\text{bottom}}(x') \right), \tag{34}$$

where $0 < x < W$, and C is an arbitrary dimensionless constant. The critical current across the junction is given by maximizing over the constant C:

$$I_c(H_0,\theta_0) = \max_C \left\{ D\int_0^W dx\, j_c^1(\theta_0)\sin(\varphi) - j_c^2\sin(2\varphi) \right\}, \tag{35}$$

where D is the width of the overlap region (i.e., DW is the junction area). At $\theta = 45^\circ$, the first harmonic contribution to the critical current density $j_c^1(\theta_0)$ is required to vanish by symmetry [55], and it has an approximately linear dependence on $\theta - 45^\circ$ close to it [consistent with the lowest-harmonic $j_c^1(\theta_0) = j_c^1(0)\cos 2\theta_0$ twist angle dependence]. At the same time, j_c^2 does not vanish at $\theta_0 = 45^\circ$ and can be approximated by a constant close to it.

For an order of magnitude estimate, it is convenient to use the average value of (C4) over x rather than the full x-dependent function. The averaging is a good approximation when $\frac{\pi W\lambda_{ab}}{d\lambda_c} \ll 1$. Furthermore, the relevant dimensionless parameter for the sum $\frac{\pi\lambda_{ab}}{d}$ can be taken much larger than 1 for flake thicknesses below 100 nm [48], while $\lambda_{ab} \sim 0.2$ μm [78,80]. On the other hand, as is evident from (C4), for $\frac{\pi W\lambda_{ab}}{d\lambda_c} \gg 1$, the inhomogeneities are confined to a region much smaller than the junction length W and can be neglected. As is shown below, the same is true if an average over x is taken. We will further assume that $\frac{\pi L\lambda_{ab}}{d\lambda_c} \gg 1$ for in-line geometry.

The dependence $\varphi(x)$ is then given by

$$-\varphi(x) \approx \frac{2\pi H_0 d_{\text{eff}} x}{\Phi_0} + C, \tag{36}$$

where

$$d_{\text{eff}} \equiv s + \frac{\lambda_{ab}^2}{W}\int_0^W dx \left(\frac{\partial H}{\partial z}\bigg|_{\text{top}}(x) - \frac{\partial H}{\partial z}\bigg|_{\text{bottom}}(x) \right) \approx s + \sum_{i=1,2}\lambda_{ab}\tanh\frac{d_i}{2\lambda_{ab}} + \delta d_{i,\text{edge}}, \tag{37}$$

where $\delta d_{i,\text{edge}}$ depends on the device geometry. For the in-line device geometry in Fig. 10(a) we have

$$\delta d_{i,\text{edge}}^{\text{in-line}} \approx -\frac{4d_i}{\pi^2}\sum_{n=0}^{\infty}\frac{1}{(2n+1)^3}\frac{1-\exp\left(-(2n+1)\frac{W\pi\lambda_{ab}}{d_i\lambda_c}\right)}{\frac{W\pi\lambda_{ab}}{d_i\lambda_c}}, \tag{38}$$

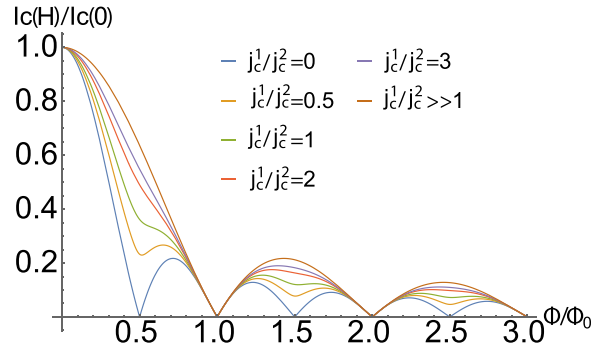

FIG. 12. Critical current vs flux displaying a Fraunhofer pattern changing its period due to the second harmonic. Dependence of the critical current on the flux threading the effective junction is $\Phi = H_0 W d_{\text{eff}}$ for different ratios of the first and second harmonic critical currents. The topological transition occurs at $j_c^1 = 2j_c^2$ [for $j_c^{1,2} > 0$ in Eq. (35)].

whereas for the vertical device geometry in Fig. 10(b) we obtain

$$\delta d_{i,\text{edge}}^{\text{vertical}} \approx -\frac{4d_i}{\pi^2}\sum_{n=0}^{\infty}\frac{1}{(2n+1)^3}\frac{\tanh\left((2n+1)\frac{W\pi\lambda_{ab}}{2d_i\lambda_c}\right)}{\frac{W\pi\lambda_{ab}}{2d_i\lambda_c}}. \tag{39}$$

Importantly, for either geometry of the junction we find that this result depends on only two dimensionless parameters: $\frac{d_i}{2\lambda_{ab}}$ and $\frac{W\pi\lambda_{ab}}{d\lambda_c}$, and not on the twist angle. The distinction between two junction geometries in Fig. 10 is purely quantitative in this regime, and the discussion below applies to both cases.

For a purely first harmonic current-phase relation [i.e., $j_c^2 = 0$ in (35)], one obtains then the conventional Fraunhofer pattern, with the first zero being at a field

$$H_0^{(1)} = \frac{\Phi_0}{W d_{\text{eff}}}, \tag{40}$$

which allows us to extract the value of d_{eff} from the experimentally observed Fraunhofer pattern. Note that in the opposite case, $j_c^1 = 0$ (i.e., at $\theta_0 = 45^\circ$), the first zero in the pattern occurs at

$$H_0^{(2)} = \frac{\Phi_0}{2W d_{\text{eff}}}, \tag{41}$$

which implies a d_{eff} value that is twice as small for the same Fraunhofer pattern. When both j_c^1 and j_c^2 are nonzero, the dependence $I_c(H)$ obtained from Eq. (35) interpolates between the two limits, as is shown in Fig. 12. Particularly sensitive are the odd-numbered zeros of the second harmonic pattern, which are visibly lifted by a nonzero j_c^1. In Fig. 13, this lifting is demonstrated more quantitatively. Indeed, for $j_c^1 \gtrsim 2j_c^2$ the values are almost indistinguishable from those at $j_c^2 = 0$. The resulting pattern does not change under $j_c^2 \to -j_c^2$. As has been shown in Sec. IV, such a sign reversal can occur as a result of strong interface inhomogeneity. In this case, the state at $2|j_c^2| > j_c^1$ is topologically trivial and does not break time reversal, as the free-energy minimum in the absence of field is at $\varphi = 0$ [46]. Consequently, while the Fraunhofer pattern can detect the presence of a second harmonic in CPR, it does imply directly the topological ground state of the system. We note that this result follows from the linear dependence

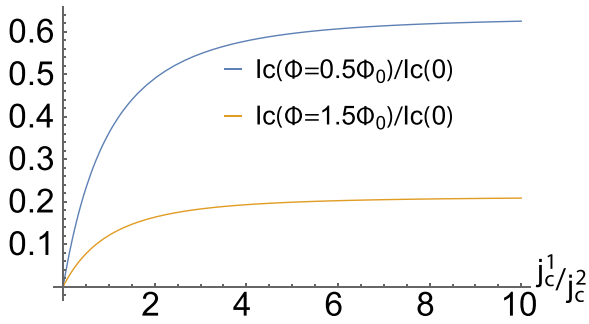

FIG. 13. Lifting the nodes of the second harmonic Fraunhofer pattern. Dependence of the critical current at half-integer flux values on the ratio between j_c^1 and j_c^2.

of the phase on the coordinate x, Eq. (36), and it does not follow from (35) for arbitrary $\varphi(x)$. On the other hand, a nonlinear dependence of the phase φ on the coordinate x would also result in deviations from the Fraunhofer pattern. As the experimental dependencies appear close to the usual Fraunhofer pattern [48], we assume that (36) holds. This implies that to determine the topological nature of the twisted system requires additional experimental measurements, e.g., the thermal Hall effect [81].

Note that d_{eff} can be temperature-dependent via the penetration depths $\lambda_{ab/c}(T)$, which have to diverge at T_c. However, the dependence on $\frac{d_i}{2\lambda_{ab}(T)}$ can be neglected, as can be seen from using the lower bound for $\lambda_{ab}(0) \gtrsim 0.21$ μm [78] and thickness $d \lesssim 100$ nm. We find that $0.49 d_i < d_i \frac{\lambda_{ab}(0)}{d_i} \tanh \frac{d_i}{2\lambda_{ab}(0)} \leqslant d_i/2$, i.e., a variation below 1%, much less than the one observed in the experiment [48]. Thus, we take $\lambda_{ab} \tanh \frac{d_i}{2\lambda_{ab}} \to d_i/2$ in (37).

While d_{eff} can depend on the device geometry and temperature, Fig. 11 suggests that robust evidence of the second harmonic in CPR can be obtained for a single device with a twist angle close to $\theta_0 = 45^\circ$. In particular, even if the cotunneling contribution, Eq. (7), leading to the second harmonic in CPR, is dominant at low T, it has to become negligible with respect to the usual tunneling current close to T_c (i.e., a transition from I to II occurs on heating). The accompanying lifting of the odd-numbered nodes in the Fraunhofer pattern on heating (Fig. 12) represents unambiguous evidence that first and second harmonic coexist in CPR.

Overall, we have shown that for twisted flakes of d-wave superconductors, a clear Fraunhofer pattern appears close to $\theta_0 = 45^\circ$ twist, with features indicating the presence of a second harmonic in the CPR. Away from $\theta_0 = 45^\circ$ as discussed in Appendix C 3, the Fraunhofer pattern will be smeared progressively due to the importance of the magnetic field generated by the twist junction itself.

B. Shapiro steps

Another quantity that can be used to study the CPR is the current-voltage characteristic of the junction under a microwave drive. A combination of DC and AC current drive results in the appearance of Shapiro steps in the IV characteristic [74,82], i.e., regions where voltage is independent of the DC current. In particular, the finite-voltage Shapiro steps in the presence of a current can determine the periodicity of the CPR [83,84]. Here, we assume that the magnetic field is absent and $\lambda_J \gg W$ such that the spatial variation of the phase difference across the junction φ can be neglected, as well as the effects of the bulk of the flakes. We will focus on the regime close to T_c, where the quasiparticle resistance is low due to the smallness of the gap, and we assume the capacitance effects to be negligible (i.e., such that the Stewart-McCumber parameter [82] $\beta_c = 2eI_cR^2C/\hbar \ll 1$, R and C being the resistance and capacitance of the junction). In this limit, the junction dynamics is overdamped (which is reflected in the absence of hysteresis in the IV characteristic) and is described by the RSJ model [74,82]:

$$\partial_{\overline{\tau}}\varphi + \overline{I_c^1}\sin\varphi + \overline{I_c^2}\sin 2\varphi = \overline{I}_0 + \overline{I}_{rf}\sin(\omega_r\tau), \tag{42}$$

where we used dimensionless parameters $\overline{\tau} = \frac{2eR(|I_c^1|+|I_c^2|)\tau}{\hbar}$, $\overline{I_c^{1,2}}, \overline{I_{0,\text{rf}}} = I_c^{1,2}, I_{c,0,\text{rf}}/(|I_c^1| + |I_c^2|)$. The DC voltage across the junction can be found from the Josephson relation

$$V = \left\langle \frac{\hbar}{2e}\partial_\tau\varphi \right\rangle_\tau, \tag{43}$$

where $\langle\cdots\rangle_\tau$ is the value averaged over time for $\overline{\tau} \gg 1$.

In Fig. 14, we present the current-voltage characteristics obtained from Eq. (42) for varying strengths of the AC driving current $\overline{I_{\text{rf}}}$ and second harmonic of the CPR. In the absence of the second harmonic, Fig. 14(a), clear Shapiro steps emerge at $V_n = n * \hbar\omega_r/2e$ as is expected for conventional Josephson junctions [74,82]. The presence of the second harmonic, Figs. 14(b) and 14(c), results in the appearance of the Shapiro steps at half-integer values of the voltage: $V_{n+1/2} = (n + 1/2) * \hbar\omega_r/2e$. For strongly second harmonic character, Fig. 14(c), the half-steps appear for all n already at weak driving. On the other hand, when first and second harmonics coexist, Fig. 14(b), the lowest half-integer step appears clearly for sufficiently strong driving and is smaller than the numerical current discretization step at weaker ones. The half-integer steps of higher order, however, are visible at weaker drives.

Overall, one observes that the half-integer Shapiro steps provide a qualitative signature of the second harmonic contribution to CPR for an overdamped junction. At the same time, the widths of individual steps show a complex dependence of the amplitude of the AC drive. These features can be understood analytically as explained in Appendix D.

In Fig. 15, we present the widths of the first few Shapiro steps obtained from Eq. (D2) as a function of $\overline{v}$. The width of the zeroth Shapiro step, Fig. 15(a) (equal to the critical current of the junction), shows a similar behavior to the Fraunhofer patterns, Fig. 12, in the sense that the coexistence of two harmonics leads to the lifting of the nodes in the dependence. In contrast to that result, actual nodes are observed only when a single harmonic is strictly dominant, making the absence of nodes in $I_0(\overline{v})$ a signature of the coexistence of harmonics.

The first Shapiro step width, Fig. 15(b), displays a qualitatively different (nonlinear) behavior at low $\overline{v}$ for the second harmonic being dominant. Finally, the width of the half-integer Shapiro steps, Fig. 15(c), is directly proportional to $|I_c^2|$ and can be used to extract its value.

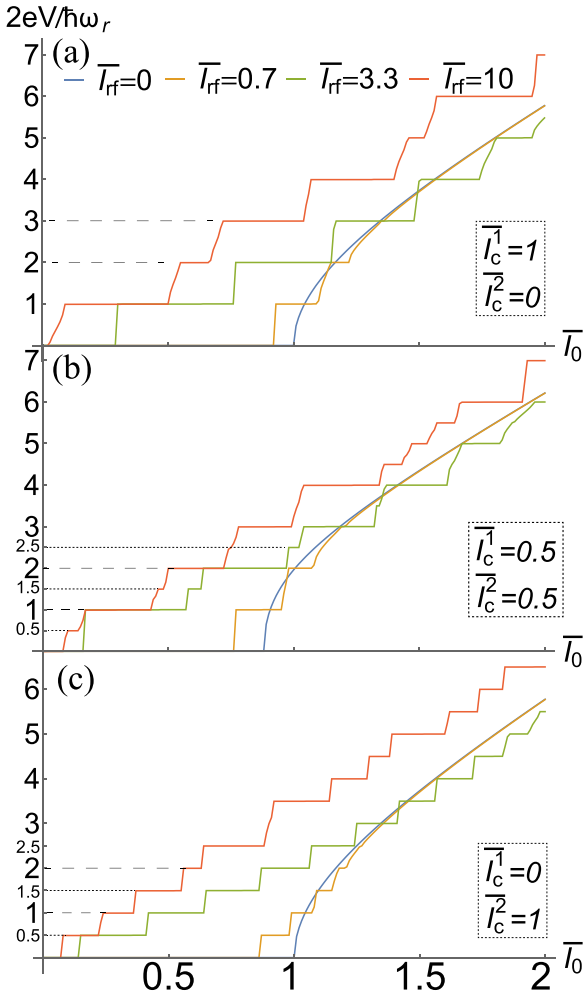

FIG. 14. Shapiro steps for a current-driven twist junction with a two-component CPR. Current-voltage characteristics for varying strength of the AC driving current $\overline{I}_{\rm rf}$ for (a) $\overline{I}_c^1 = 1$, $\overline{I}_c^2 = 0$; (b) $\overline{I}_c^1 = 0.5$, $\overline{I}_c^2 = 0.5$; (c) $\overline{I}_c^1 = 0$, $\overline{I}_c^2 = 1$. When the second harmonic in CPR is present [(b),(c)], current steps at half-integer values of voltage develop.

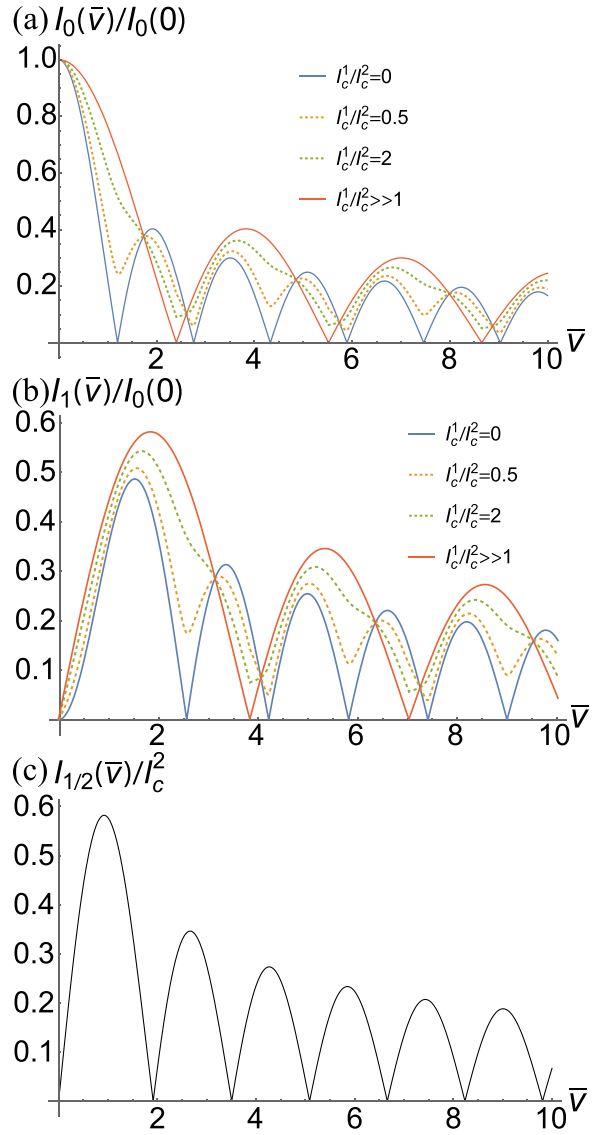

FIG. 15. Shapiro step width for a voltage-driven twist junction with a two-component CPR. Normalized widths of the (a) zeroth, (b) first, and (c) one-half Shapiro steps as a function of the amplitude of the AC voltage. The appearance of the first harmonic lifts the nodes in [(a), (b)], similar to the Fraunhofer pattern in magnetic field, Fig. 12. The one-half step width is directly related to the magnitude of the second harmonic in CPR, Eq. (D2).

VI. CONCLUSIONS

In this article, we have studied the Josephson effect in twisted bilayers of nodal superconductors and analyzed experimental setups that can be used to measure the current-phase characteristics of these devices. We have demonstrated that one can reveal the fingerprints of the predicted emergent physics in these systems using widely available experiments.

In particular, the temperature dependence of the critical current is quite generally expected to have a nonmonotonic form due to the negative contribution of the near-nodal region in momentum space. The critical current is strongly suppressed on increasing the twist angle, with the precise form reflecting the Fermi surface geometry, momentum dependence of the tunneling, and roughness of the interface. At $\theta_0 = 45^\circ$, the critical current reaches a nonzero minimum due to the Cooper pair cotunneling processes. The latter can lead to the presence of a transition into a topological phase, spontaneously breaking time-reversal symmetry, which can be suppressed for strong interface roughness.

Dependence of the critical current on magnetic field has been studied including the effects of the sample geometry and for finite-thickness flakes forming the junction. At $\theta_0 = 45^\circ$, we have demonstrated that a clear Fraunhofer pattern with halved period should be observed; at elevated temperatures close to $\theta_0 = 45^\circ$ the odd-numbered zeros are lifted, suggesting a robust signature of the coexistence of tunneling and cotunneling of Cooper pairs. Further away from $\theta_0 = 45^\circ$ the Fraunhofer pattern is shown to vanish due to self-field effects, and we have calculated the critical current density for this crossover. Lastly, we demonstrated how the presence of

half-integer Shapiro steps under microwave drive and their widths can be used to detect the cotunneling contribution to the CPR.

Our results reproduce the main features observed in the recent experiments on twist junctions of high-T_c cuprates [48–50,60]. This includes the $I_c \sim \cos(2\theta_0)$ dependence of the critical current, its nonmonotonic temperature dependence with a maximum at nonzero temperature, the emergence of a Fraunhofer-like dependence on magnetic field close to $\theta_0 = 45^\circ$, and fractional Shapiro steps in the presence of a microwave drive. The latter two signatures appear consistent with the critical current being dominated by Cooper pair cotunneling, necessary for the realization of the topological state near 45°.

Note added. Various aspects of the Josephson effect in twisted cuprates have also been considered in a recent study [57]. The results in [57] are in agreement with the ones presented here when there is overlap.

ACKNOWLEDGMENTS

We thank Marcel Franz, Stephan Plugge, and Tarun Tummuru for useful discussions and collaborations on related work. P.A.V. was supported by a Rutgers Center for Material Theory Abrahams Postdoctoral Fellowship, and J.H.P. is partially supported by the Air Force Office of Scientific Research under Grant No. FA9550-20-1-0136, NSF CAREER Grant No. DMR-1941569, and the Alfred P. Sloan Foundation through a Sloan Research Fellowship. P.A.V. and J.H.P. acknowledge the Aspen Center for Physics where part of this work was performed, which is supported by National Science Foundation Grant No. PHY-1607611. This work was partially supported by a grant from the Simons Foundation (P.A.V.). N.P. acknowledges the Deutsche Forschungsgemeinschaft (DFG452128813) for partial support with the project. P.K. acknowledge the support from the AFOSR (FA9550-25-1-0019), and S.Y.F.Z and X.C acknowledge the support from NSF (DMR-2105048).

APPENDIX A: $I_c^{(2)}(\varphi, T, \theta_0)$ FOR A BILAYER UNIT CELL

In Sec. III B we analyzed a model appropriate for BSCCO including its Fermi surface and momentum-dependent interlayer tunneling. However, this model was still a simplification as it considered twisting of two single CuO_2 layers whereas the unit cell of BSCCO is known to contain two CuO_2 planes. Consequently, a twisted bilayer of BSCCO is actually a twisted double bilayer. Here we demonstrate that the bilayer unit cell results in observations very similar to those in the main text, Sec. III B. In Fig. 16(a), a schematic of the four Fermi surfaces of such a system is given: in addition to the tunneling at the interface $t(\mathbf{k}, \mathbf{k}')$ one has to take into account the tunneling within each bilayer unit cell, $t_b(\mathbf{k})$. We assume the latter to be momentum-conserving; furthermore, the momentum dependence of $t_b(\mathbf{k})$ for BSCCO is approximately given by [66]

$$t_b(\mathbf{k}) = t_b^0(\cos k_x - \cos k_y)^2/4, \tag{A1}$$

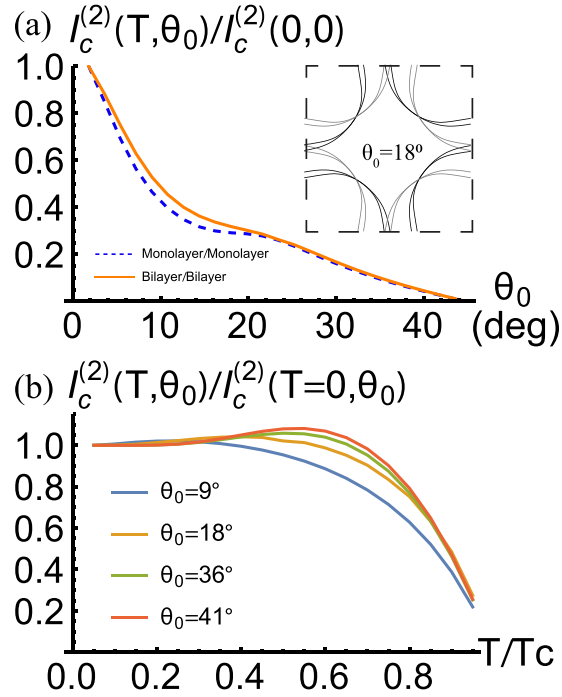

FIG. 16. Second-order approximation for the critical current $I_c^{(2)}(T, \theta_0)$ for a bilayer unit cell. (a) Schematic of a twisted double bilayer: $t_b(\mathbf{k})$ is the tunneling within a single bilayer (modeling the unit cell of BSCCO), while at the interface between twisted bilayers the tunneling is $t(\mathbf{k}, \mathbf{k}')$. Part (b) displays the twist angle θ_0 dependence of $I_c^{(2)}$ compared to that for a single-layer unit cell (blue dashed, Fig. 4) Inset: Fermi surface [cf. Fig. 4(a)] for the twisted double bilayer at $\theta_0 = 18^\circ$. The crossing of the Fermi surfaces in the antinodal region occurs at lower twists than in the twisted bilayer. (c) The temperature T dependence of $I_c^{(2)}$ for various twist angles that displays a nonmonotonic behavior.

where $t_b^0 = 30\,\text{meV}$. To generalize Eq. (6) to the case of a double bilayer, we use Eqs. (3) and (4), where

$$\hat{G}^{-1}(i\varepsilon_n, \mathbf{k}) = \begin{bmatrix} \hat{G}_b^{-1}(i\varepsilon_n, \varphi, \mathbf{k}) & 0 \\ 0 & \hat{G}_b^{-1}(i\varepsilon_n, 0, \tilde{\mathbf{k}}) \end{bmatrix},$$

$$\hat{G}_b^{-1}(i\varepsilon_n, \varphi, \mathbf{k}) = i\varepsilon_n - \begin{bmatrix} \xi(\mathbf{k})\tau_3 + \hat{\Delta}(\mathbf{k}) & t_b(\mathbf{k})\tau_3 \\ t_b(\mathbf{k})\tau_3 & \xi(\mathbf{k})\tau_3 + \hat{\Delta}(\mathbf{k}) \end{bmatrix},$$

$$\hat{t}(\mathbf{k}, \mathbf{k}') = \begin{bmatrix} 0 & 0 & 0 & 0 \\ 0 & 0 & t(\mathbf{k}, \mathbf{k}') & 0 \\ 0 & t^*(\mathbf{k}, \mathbf{k}') & 0 & 0 \\ 0 & 0 & 0 & 0 \end{bmatrix}, \tag{A2}$$

where $\hat{\Delta}(\mathbf{k}) = \Delta(\mathbf{k})[\cos\varphi\tau_1 - \sin\varphi\tau_2]$. The results of the calculation of second-order (in t) Josephson critical current are presented in Fig. 16 (for momentum-independent tunneling at the interface) and Fig. 17 [for momentum-dependent tunneling (16) at the interface]. One observes that the results are quite similar to those in Sec. III B. The only noticeable difference is that I_c^2 appears to fall off slower for the double bilayer case at low twist angles. This can be explained by the Fermi surface geometry: due to the bilayer splitting [Fig. 16(b), inset], the bonding Fermi surfaces in the double

bilayer cross in the antinodal region at lower θ_0 than in the twisted bilayer case [Fig. 4(a), inset]. As the contribution of the antinodal region to I_c^2 is positive (see Sec. III C), this suggests that I_c^2 for the double bilayer should be larger at low twist angles (where the twisted Fermi surfaces have not crossed yet in the single bilayer), as is observed.

APPENDIX B: EVALUATING THE TUNNELING CONTRIBUTION IN THE PRESENCE OF INTERFACE ROUGHNESS

We can now perform the angular integration in Eq. (6). To do this, we rewrite (6) using Fourier series:

$$I^{(2)}(\varphi,T,\theta_0)=\frac{4e\sin\varphi}{\hbar}T\sum_{\varepsilon_n}\int\frac{kdk}{(2\pi)^2}\frac{k'dk'}{(2\pi)^2}\frac{t_0^2}{2\pi\sigma^2}e^{-\frac{(k-k')^2}{2\sigma^2}}I^{(2)}_{\rm ang}(\varepsilon_n,\theta_0,k,k'),\tag{B1}$$

where

$$\begin{aligned}I^{(2)}_{\rm ang}(\varepsilon_n,\theta_0,k,k')&=\int d\theta d\theta' e^{-\frac{(\theta-\theta')^2}{2\tilde\sigma^2}}\sum_n f_n(k)\cos 2n\theta\sum_m f_m(k')\cos 2m(\theta'+\theta_0)\\&=\pi\sqrt{2\pi\tilde\sigma^2}\sum_m f_m(k)f_m(k')e^{-2\tilde\sigma^2m^2}\cos 2m\theta_0,\end{aligned}\tag{B2}$$

where we assumed $\tilde\sigma\ll\pi$ and

$$\begin{aligned}f_{m\neq0}(k)&=\int\frac{d\theta}{\pi}\frac{\Delta(\mathbf{k})\cos(2m\theta)}{\varepsilon_n^2+\xi^2(\mathbf{k})+\Delta^2(\mathbf{k})},\\f_{m=0}(k)&=0,\end{aligned}\tag{B3}$$

are the Fourier coefficients of the anomalous Green's functions. One observes already that the nonconservation of the angular component of the momentum suppresses the oscillatory behavior of $I^{(2)}(\varphi,T,\theta_0)$ as a function of θ_0. Indeed, in (B2) the high harmonics ($n\gg\frac{1}{\tilde\sigma}$) are strongly suppressed (the precise form depends, however, on the realization of momentum smearing in the tunneling).

To make further progress analytically, we take $\xi(\mathbf{k})=\xi(k)$ and $\Delta(\mathbf{k})=\Delta(T)\cos2\theta$ as in Sec. II B and limit ourselves to the lowest terms in the Fourier series, Eq. (B2). This results in $f_0(\xi)=0$ and $f_2(\xi)=0$ [see Eq. (B3)] while

$$\begin{aligned}f_1(\xi)&=\frac{2}{\Delta(T)}\left(1-\sqrt{\frac{\varepsilon^2+\xi^2}{\varepsilon^2+\xi^2+\Delta^2(T)}}\right),\\f_3(\xi)&=\frac{2}{\Delta^3(T)}\left(-4(\varepsilon^2+\xi^2)-\Delta^2(T)+[4(\varepsilon^2+\xi^2)+3\Delta^2(T)]\sqrt{\frac{\varepsilon^2+\xi^2}{\varepsilon^2+\xi^2+\Delta^2(T)}}\right).\end{aligned}\tag{B4}$$

For smooth inhomogeneity, we assume $\hbar v_F\sigma\ll\sqrt{\Delta^2(T)+(\pi T)^2}$, which can be valid at all T. We can further simplify the result by taking the limit $\sigma\to0$ in the k,k' integral [see Eq. (B1)] to obtain

$$\begin{aligned}I^{(2)}_{\rm SI}(T,\varphi,\theta_0)&\approx\frac{et_0^2\sin\varphi k_F}{4\pi^3\hbar^2v_F}\left[i_1^{(2)}(T)\cos(2\theta_0)e^{-2\tilde\sigma^2}+i_3(T)\cos(6\theta_0)e^{-18\tilde\sigma^2}\right],\\i_1^{(2)}(T)&=T\sum_{\varepsilon_n}\int d\xi f_1^2(\xi)\approx\begin{cases}2(\log4-1), & T\to0,\\0.1\frac{\Delta^2(T)}{T_c^2}, & T\to T_c,\end{cases}\\i_3^{(2)}(T)&=T\sum_{\varepsilon_n}\int d\xi f_3^2(\xi)\approx\begin{cases}2(\log4-4/3), & T\to0,\\4\times10^{-5}\frac{\Delta^6(T)}{T_c^6}, & T\to T_c.\end{cases}\end{aligned}\tag{B5}$$

In the opposite limit of rough inhomogeneity, $\hbar v_F\sigma\gg\sqrt{\Delta^2(T)+(\pi T)^2}$, we obtain a result that is consistent with the more usual Ambegaokar-Baratoff [69] -like expression

$$\begin{aligned}I^{(2)}_{\rm RI}(T,\varphi,\theta_0)&\approx\frac{et_0^2\sin\varphi k_F}{4\pi^3\hbar^2v_F}\frac{1}{\sqrt{2\pi}\hbar v_F\sigma}\left(\tilde i_1^{(2)}(T)\cos(2\theta_0)e^{-2\tilde\sigma^2}+\tilde i_3^{(2)}(T)\cos(6\theta_0)e^{-18\tilde\sigma^2}\right),\\\tilde i_1^{(2)}(T)&=T\sum_{\varepsilon_n}\left(\int d\xi f_1(\xi)\right)^2\approx\begin{cases}6.035\Delta(T), & T\to0,\\\frac{\pi^2}{4}\frac{\Delta^2(T)}{T_c}, & T\to T_c,\end{cases}\\\tilde i_3^{(2)}(T)&=T\sum_{\varepsilon_n}\left(\int d\xi f_3(\xi)\right)^2\approx\begin{cases}0.18\Delta(T), & T\to0,\\3\times10^{-4}\frac{\Delta^2(T)}{T_c}, & T\to T_c.\end{cases}\end{aligned}\tag{B6}$$

In both cases, the $\cos(6\theta_0)$ contribution appears to be strongly suppressed numerically (in addition to the exponential suppression due to angular spread): by an almost order of magnitude at low T and by several orders of magnitude close to T_c.

We now apply similar calculations to obtain the fourth-order tunneling contribution to the critical current $I^{(4)}$ in Eq. (7). By applying the same expansion in twist angle harmonics, we obtain the following result for the leading twist-angle harmonics:

$$\begin{aligned} I^{(4)} &= I^{(4)}_{1,c}(T)\cos 2\theta_0 \sin\varphi + I^{(4)}_{2,c}(T,\theta_0)\sin 2\varphi, \\ I^{(4)}_{1,c}(T) &= -\frac{et_0^4 k_F \sigma^2 e^{-3\tilde{\sigma}^2}}{\hbar^2 v_F (2\pi)^6} i^{(4)}_1(T), \\ I^{(4)}_{2,c}(T,\theta_0) &= -\frac{et_0^4 k_F \sigma^2 e^{-4\tilde{\sigma}^2}}{\hbar^2 v_F (2\pi)^7}\left(\cos 4\theta_0 + 2e^{-4\tilde{\sigma}^2}\right) i^{(4)}_2(T), \end{aligned} \tag{B7}$$

where

$$\begin{aligned} i^{(4,\mathrm{SI})}_1(T) &= T\sum_{\varepsilon_n}\int d\xi\, f_1^2(\xi)\left(\varepsilon_n^2 - \xi^2\right) g_0^2(\xi), \\ i^{(4,\mathrm{RI})}_1(T) &= \frac{T\sum_{\varepsilon_n}\left(\int d\xi\, f_1(\xi)\right)^2\left(\int d\xi\, \varepsilon_n g_0(\xi)\right)^2}{2(\sqrt{\pi}\hbar v_F \sigma)^3}, \\ i^{(4,\mathrm{SI})}_2(T) &= T\sum_{\varepsilon_n}\int d\xi\, f_1^4(\xi), \\ i^{(4,\mathrm{RI})}_2(T) &= \frac{T\sum_{\varepsilon_n}\left(\int d\xi\, f_1(\xi)\right)^4}{2(\sqrt{\pi}\hbar v_F \sigma)^3}. \end{aligned} \tag{B8}$$

Recall that SI and RI label the smooth and rough inhomogeneity regimes, respectively, and we have introduced

$$g_0(k) = \int \frac{d\theta}{2\pi}\frac{1}{\varepsilon_n^2 + \xi^2(\mathbf{k}) + \Delta^2(\mathbf{k})}. \tag{B9}$$

APPENDIX C: SOLUTION OF THE LONDON EQUATION

1. Without self-field effects

To solve the London equation in Eq. (30) we use the variable-separation ansatz:

$$H_1(x,z) = H_{L\to\infty}(z) + \sum_{n>0} C_n \frac{\cosh\left(\frac{x}{\lambda_c}\sqrt{\left(\frac{(2n+1)\pi\lambda_{ab}}{d}\right)^2+1}\right)}{\cosh\left(\frac{L}{2\lambda_c}\sqrt{\left(\frac{(2n+1)\pi\lambda_{ab}}{d}\right)^2+1}\right)}\cos\frac{(2n+1)\pi z}{d}, \tag{C1}$$

where we use $H(x,z) = H(x,-z)$ and $H|_{z=\pm d/2} = H_0$ and $H|_{z=\pm L/2} = H_0$. We denote this solution as $H_1(x,z)$ to highlight that the self-field of the twist junction has been neglected. To determine the coefficients C_n we use the boundary conditions at the ends of the flake $H|_{x=\pm L/2} = H_0$:

$$C_n = \frac{2H_0}{d}\int_{-d/2}^{d/2} dz\left(1 - \frac{\cosh\frac{z}{\lambda_{ab}}}{\cosh\frac{d}{2\lambda_{ab}}}\right)\cos\frac{(2n+1)\pi z}{d} = \frac{4H_0(-1)^n}{(2n+1)\pi} - \frac{4H_0(-1)^n\frac{(2n+1)\pi\lambda_{ab}^2}{d^2}}{\left(\frac{(2n+1)\pi\lambda_{ab}}{d}\right)^2+1} = \frac{4H_0(-1)^n}{(2n+1)\pi}\frac{1}{\left(\frac{(2n+1)\pi\lambda_{ab}}{d}\right)^2+1}, \tag{C2}$$

where we used $\int \cosh z\cos az = \frac{a\cosh z\sin az + \sinh z\cos az}{a^2+1}$. Finally, the full solution for $H_1(x,z)$ for $H_j(x) = 0$ is given by

$$H_1(x,z) = H_0\frac{\cosh\frac{z}{\lambda_{ab}}}{\cosh\frac{d}{2\lambda_{ab}}} + H_0\sum_{n=0}^{\infty}\frac{4(-1)^n}{(2n+1)\pi}\frac{\cos\frac{(2n+1)\pi z}{d}}{\left(\frac{(2n+1)\pi\lambda_{ab}}{d}\right)^2+1}\frac{\cosh\left(\frac{x}{\lambda_c}\sqrt{\left(\frac{(2n+1)\pi\lambda_{ab}}{d}\right)^2+1}\right)}{\cosh\left(\frac{L}{2\lambda_c}\sqrt{\left(\frac{(2n+1)\pi\lambda_{ab}}{d}\right)^2+1}\right)}. \tag{C3}$$

The relevant quantity that enters Maxwell's equations at the junction's edges is

$$\pm\left.\frac{\partial H_1}{\partial z}(x)\right|_{z=\pm d/2} = \frac{H_0}{\lambda_{ab}}\tanh\frac{d}{2\lambda_{ab}} - \frac{4H_0}{d}\sum_{n=0}^{\infty}\frac{1}{\left(\frac{(2n+1)\pi\lambda_{ab}}{d}\right)^2+1}\frac{\cosh\left(\frac{x}{\lambda_c}\sqrt{\left(\frac{(2n+1)\pi\lambda_{ab}}{d}\right)^2+1}\right)}{\cosh\left(\frac{L}{2\lambda_c}\sqrt{\left(\frac{(2n+1)\pi\lambda_{ab}}{d}\right)^2+1}\right)}. \tag{C4}$$

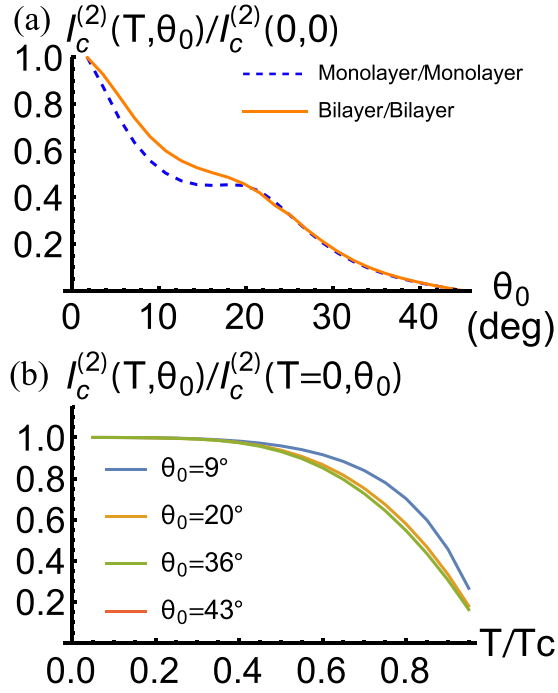

FIG. 17. Second-order approximation for the critical current $I_c^{(2)}(T,\theta_0)$ for a bilayer unit cell and momentum-dependent tunneling (16). (a) Displays the twist angle θ_0 dependence of $I_c^{(2)}$ compared to that for a single-layer unit cell (blue dashed, Fig. 4). (b) The temperature T dependence of $I_c^{(2)}$ for various twist angles that displays a monotonic behavior.

2. Including self-field effects

We can write the solution as $H(x,z) = H_1(x,z) + \delta H(x,z)$, where $H_1(x,z)$ is given by (C3). $\delta H(x,z)$ satisfies zero boundary conditions except for the surface of the junction, where it is equal to $H_j(x)$. The solution can be obtained by a variable separation ansatz that yields

$$\delta H(x,z) = \sum_{n\neq 0} h_n \frac{\sinh\frac{(d/2-z)\sqrt{1+\lambda_c^2k_n^2}}{\lambda_{ab}}}{\sinh\frac{d\sqrt{1+\lambda_c^2k_n^2}}{\lambda_{ab}}}\sin[k_n(x+W/2)],$$
$$h_n = \frac{1}{W}\int_{-W/2}^{W/2} dx H_j(x)\sin[k_n(x+W/2)], \tag{C5}$$

where $k_n = \frac{\pi n}{W}$. Next, we need to express the extra field in the junction via the phase difference (32). In particular, we can use the result of Sec. V A 1 and include the correction due to the Josephson self-field as

$$\varphi(x) \to \varphi(x) + \delta\varphi(x),$$
$$\delta\varphi(x) \equiv \sum_{n>0}\delta\varphi_n\cos\left(\frac{\pi nx}{W}+\frac{\pi n}{2}\right), \tag{C6}$$

where $\varphi(x)$ is given by Eqs. (34) and (36). From Eq. (32) we find

$$\delta h_n = -\frac{\Phi_0}{2\pi}\frac{k_n\delta\varphi_n}{s+\sum_{i=1,2}\lambda_{ab}\sqrt{1+k_n^2\lambda_c^2}\coth\frac{d\sqrt{1+k_n^2\lambda_c^2}}{\lambda_{ab}}}. \tag{C7}$$

3. Away from $\theta_0 = 45°$: Crossover to the long-junction limit

Away from $\theta_0 = 45°$, the critical current density of the twist junction grows strongly and one cannot ignore the effect of this current on magnetic field anymore.

To start with a concrete but simple example, we first discuss the case of two monolayers of a nodal superconductor in magnetic field (i.e., both flakes in Fig. 10 being monolayers). The current in the monolayer flowing along x is given by [77]

$$j_x(x,z) = -\frac{c\Phi_0 s'}{8\pi^2\lambda_{ab}^2}\left(\partial_x\Phi_{1,2}(x)+\frac{2\pi}{\Phi_0}A_x\right)\delta(z-z_{1,2}), \tag{C8}$$

where s' is the monolayer thickness and $z_{1,2}$ is its coordinate along z (where $z_1 - z_2 = s$), and $\Phi_0 = \pi\hbar c/|e|$ is the flux quantum. We denote the magnetic field between the monolayers as $H_0 + H_j(x)$ (outside it is equal to H_0). Integrating Maxwell's equation $-\frac{\partial H}{\partial z} = \frac{4\pi}{c}j_x$ across each flake and subtracting the results, we get

$$H_j(x) = -\frac{s'\Phi_0}{4\pi\lambda_{ab}^2}\left(\partial_x(\Phi_1-\Phi_2)\right.$$
$$\left.+\frac{2\pi}{\Phi_0}[A_x(z=z_1)-A_x(z=z_2)]\right). \tag{C9}$$

Assuming the magnetic field variations occur at a scale much larger than s, we can further bring this equation to the form

$$H_j(x) \approx -\frac{\frac{\Phi_0}{2\pi}\partial_x\varphi}{\frac{2\lambda_{ab}^2}{s'}+s} - \frac{H_0\frac{s's}{2\lambda_{ab}^2}}{1+\frac{s's}{2\lambda_{ab}^2}}, \tag{C10}$$

where we introduced the gauge-invariant phase difference across the junction:

$$\varphi(x) = \Phi_1(x) - \Phi_2(x) + \frac{2\pi}{\Phi_0}\int_{z_1}^{z_2} A_z dz. \tag{C11}$$

Finally, we can get a closed equation for $\varphi(x)$ in the case of a twisted monolayers (ml) using $\frac{\partial H}{\partial x} = -\frac{4\pi}{c}[j_c^{(1)}\sin(\varphi) + j_c^{(2)}\sin(2\varphi)]$:

$$\partial_{xx}\varphi = \frac{\sin(\varphi)}{\lambda_{J1,\mathrm{ml}}^2} + \frac{\sin(2\varphi)}{\lambda_{J2,\mathrm{ml}}^2},$$
$$\lambda_{J1(2),\mathrm{ml}}^2 = \frac{c|\Phi_0|}{8\pi^2 j_c^{[1(2)]}\left(\frac{2\lambda_{ab}^2}{s'}+s\right)}. \tag{C12}$$

For $s' = s$, $\lambda_{ab} \gg s$, and $j_c^{(1)} = \frac{c|\Phi_0|}{8\pi^2 s\lambda_c^2}$, we recover the known result $\lambda_{J1,\mathrm{ml}}^2 = s^2\gamma^2/2$ [77], where $\gamma = \lambda_c/\lambda_{ab}$. The boundary conditions for this equation are determined by the external field and the current in the in-plane geometry.

As has been shown above, the Josephson length for twisted monolayers $\lambda_{J1,\mathrm{ml}}$ decreases away from $\theta_0 = 45°$ rapidly and hence the second harmonic term in (C12) can be neglected, reducing it to the usual equation describing a long Josephson junction [73]. The solution of this problem is well-known and we shall not reproduce it here: for $\lambda_{J1,\mathrm{ml}} \lesssim W$ while the critical current is still suppressed by field, no clear Fraunhofer pattern is expected: in particular, $I_c(H)$ exhibits no zeros at finite fields [73].

We can now discuss the case of finite-thickness flakes. To allow for an analytical closed-form expression, we will focus on the vertical junction geometry, Fig. 10(b). To include the

effects of the junction self-field, we will follow an approach similar to Ref. [85]. In particular, we first solve Eq. (30) for an arbitrary function $H_j(x)$ and then reexpress the magnetic field inside the junction via the phase difference $\varphi(x)$ using Eq. (32). Finally, using $\frac{\partial H}{\partial x} = j_c^{(1)} \sin(\varphi)$ (we neglect the second harmonic here assuming θ_0 to be sufficiently far from $\theta_0 = 45^\circ$), we obtain

$$\int_{-W/2}^{W/2} K(x-x')\partial_{x'x'}\varphi(x') = \frac{8\pi^2 j_c^{(1)}}{c\Phi_0} \sin[\varphi_0(x) + \delta\varphi(x)], \tag{C13}$$

where the kernel $K(x-x')$ is given by

$$K(x,x') = \frac{1}{W}\sum_{n>0} \frac{\cos[k_n(x+L/2)]\cos[k_n(x'+L/2)]}{s + \sum_{i=1,2}\lambda_{ab}\sqrt{1+k_n^2\lambda_c^2}\coth\frac{d\sqrt{1+k_n^2\lambda_c^2}}{\lambda_{ab}}}. \tag{C14}$$

The expression (C13) can then be analyzed in several limiting cases. In particular,

$$K(x,x') = \begin{cases} \frac{\delta(x-x')}{s}, & s \gg \lambda_{ab}, \\ \frac{\delta(x-x')}{s+\sum_i \frac{\lambda_{ab}^2}{d_i}}, & d_i \ll \lambda_{ab}. \end{cases} \tag{C15}$$

For both of these cases, the resulting Josephson length is given by

$$\lambda_{J,\mathrm{fl}}^2 = \frac{c\Phi_0}{8\pi^2 j_c^{(1)}\left(s + \sum_i \frac{\lambda_{ab}^2}{d_i}\right)}. \tag{C16}$$

Importantly, the reduction of the effective thickness, evident in Eq. (36), does not show up here in the same way as for conventional Josephson junctions. Thus, Eq. (C16) implies that the limit on the critical current density for the observation of the Fraunhofer pattern is given by

$$j_c^{(1)} < \frac{c\Phi_0}{8\pi^2 W^2\left(s + \sum_i \frac{\lambda_{ab}^2}{d_i}\right)}. \tag{C17}$$

For $d \gg \lambda_{ab}$, the problem becomes manifestly nonlocal; however, Eq. (C16) can be used as an order of magnitude estimate in this case. For $W \ll \lambda_c$, on the other hand, the relevant lengthscale is of the order $\lambda_{J,\mathrm{fl}}^2 \sim \frac{c\Phi_0}{j_c^{(1)}\lambda_{ab}\lambda_c/W}$. The critical value of the Josephson current (for the observation of the Fraunhofer pattern) is of the order $\frac{c\Phi_0}{W\lambda_{ab}\lambda_c}$, smaller than the one in Eq. (C17) (assuming $s \ll \lambda_{ab}^2/d_i$) by $\sim W\lambda_{ab}/(d\lambda_c)$.

APPENDIX D: ADDITIONAL DETAILS ON SHAPIRO STEPS

To appreciate the details of this effect analytically, we consider the simplified voltage-driven model [74], where a time-dependent voltage (instead of current) $V(\tau) = V + v\sin\omega_r\tau$ is driven through the junction. Using the second Josephson relation, one finds [74]

$$\varphi(\tau) = \omega_f\tau + \overline{v}\sin\omega_r\tau + \varphi_0, \qquad \omega_f = \frac{2eV}{\hbar}, \quad \overline{v} = \frac{v}{\frac{\hbar\omega_r}{2e}}, \tag{D1}$$

where φ_0 is a constant determined by the initial conditions. Introducing $\varphi(\tau)$ into the two-component Josephson CPR and

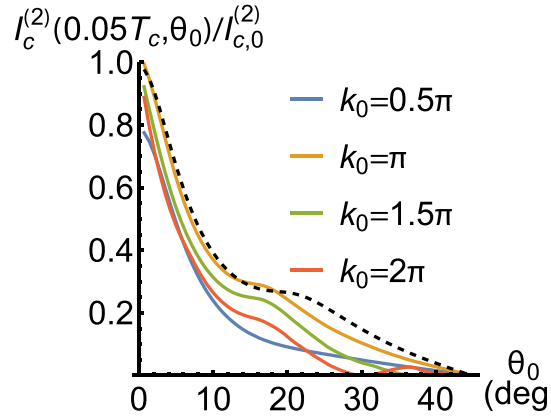

FIG. 18. Influence of higher Brillouin zones on the critical current. Colored lines represent the second-order critical current in Eq. (6), with a tunneling that has a smooth momentum cutoff k_0, (E1). The black dashed line is the first Brillouin zone restricted result from Fig. 4. The results are normalized to $I_{c,0}^{(2)}$—the critical current value at zero twist and $T/T_c = 0.01$ in Fig. 4.

using expansion in Bessel functions, we obtain

$$\begin{aligned} I_J(t) &= I_c^1 \sin\varphi(\tau) + I_c^2 \sin 2\varphi(\tau) \\ &= \sum_{k=-\infty}^{\infty} I_c^1 J_k(\overline{v})\sin[(\omega_f + k\omega_r)\tau + \varphi_0] \\ &\quad + I_c^2 J_{2k}(2\overline{v})\sin[(2\omega_f + k\omega_r)\tau + 2\varphi_0]. \end{aligned} \tag{D2}$$

We now investigate the effects resulting from the coexistence of two harmonics in the CPR. From Eq. (D2) it follows that for $V = V_n = n * \frac{\hbar\omega_r}{2e}$ or $V = V_{n+1/2} = (n+1/2) * \frac{\hbar\omega_r}{2e}$ [i.e., $\omega_f = n\omega_r$ or $(n+1/2)\omega_r$] terms with $k = -2n$ or $k = -(2n+1)$, respectively, yield a time-independent contribution to current. This contribution will add to the DC quasiparticle current resulting in a finite current step [74]. The value of this DC Josephson contribution depends on φ_0; the full width of the current step is consequently determined by its maximum value:

$$\begin{aligned} \delta I_n &= \max_{\varphi_0} \left| I_c^1 J_n(\overline{v})\sin[\varphi_0] + I_c^2 J_{2n}(2\overline{v})\sin[2\varphi_0] \right|, \\ \delta I_{n+1/2} &= \left| I_c^2 J_{2n+1}(2\overline{v}) \right|. \end{aligned} \tag{D3}$$

Note that this expression is insensitive to the sign of I_c^2. As with the Fraunhofer patterns, this means that this measure does not distinguish between the signs of I_c^1 and I_c^2 being the same or different.

APPENDIX E: UMKLAPP PROCESSES AND HIGHER BRILLOUIN ZONES

In this Appendix, we consider the influence of umklapp processes in the tunneling amplitude, i.e., the influence of higher Brillouin zones on the critical current $I_c^{(2)}$ in Eq. (6). To do so systematically, we introduce tunneling with a smooth momentum cutoff,

$$t(\mathbf{k},\mathbf{k}') = t_0\delta_{\mathbf{k},\mathbf{k}'}\frac{e^{-\mathbf{k}^2/k_0^2}}{\pi k_0^2}, \tag{E1}$$

and we perform the momentum integrals in (6) up to momentum $10k_0$ for convergence. We use the dispersion and

parameters given in Sec. III B with momentum-independent tunneling.

The results are presented in Fig. 18 for low temperature $T = 0.05T_c$ as a function of the twist angle θ_0. One observes that for $k_0 = \pi$, where tunneling roughly covers the first Brillouin zone, the results are close to the ones obtained by restricting the tunneling to the first Brillouin zone (black dashed line).

The main features of the results presented in the main text remain rather robust even if the tunneling range is changed: a pronounced decrease of critical current from $\theta_0 = 0^\circ$ to 45°, where it vanishes. However, the finer features, such as a "step" at about 20°, get weak at low k_0, whereas a much stronger suppression (including additional zeros) close to 45° occurs for $k_0 > \pi$. The latter case is, however, rather unphysical since the tunneling is expected to decay with momenta of order $1/c$, c being the c-axis lattice constant [19]. Therefore, we suggest that the additional zeros of the second-order critical current are unlikely to be realized in real materials.

[1] A. K. Geim and I. V. Grigorieva, Van der Waals heterostructures, Nature (London) **499**, 419 (2013).

[2] N. Mounet, M. Gibertini, P. Schwaller, D. Campi, A. Merkys, A. Marrazzo, T. Sohier, I. E. Castelli, A. Cepellotti, G. Pizzi *et al.*, Two-dimensional materials from high-throughput computational exfoliation of experimentally known compounds, Nat. Nanotechnol. **13**, 246 (2018).

[3] K. Kim, M. Yankowitz, B. Fallahazad, S. Kang, H. C. Movva, S. Huang, S. Larentis, C. M. Corbet, T. Taniguchi, K. Watanabe *et al.*, van der Waals heterostructures with high accuracy rotational alignment, Nano Lett. **16**, 1989 (2016).

[4] G. Ni, H. Wang, B.-Y. Jiang, L. Chen, Y. Du, Z. Sun, M. Goldflam, A. Frenzel, X. Xie, M. Fogler *et al.*, Soliton superlattices in twisted hexagonal boron nitride, Nat. Commun. **10**, 1 (2019).

[5] C. Woods, P. Ares, H. Nevison-Andrews, M. Holwill, R. Fabregas, F. Guinea, A. Geim, K. Novoselov, N. Walet, and L. Fumagalli, Charge-polarized interfacial superlattices in marginally twisted hexagonal boron nitride, Nat. Commun. **12**, 347 (2021).

[6] Y. Cao, V. Fatemi, A. Demir, S. Fang, S. L. Tomarken, J. Y. Luo, J. D. Sanchez-Yamagishi, K. Watanabe, T. Taniguchi, E. Kaxiras, R. C. Ashoori, and P. Jarillo-Herrero, Correlated insulator behaviour at half-filling in magic-angle graphene superlattices, Nature (London) **556**, 80 (2018).

[7] Y. Cao, V. Fatemi, S. Fang, K. Watanabe, T. Taniguchi, E. Kaxiras, and P. Jarillo-Herrero, Unconventional superconductivity in magic-angle graphene superlattices, Nature (London) **556**, 43 (2018).

[8] M. Yankowitz, S. Chen, H. Polshyn, Y. Zhang, K. Watanabe, T. Taniguchi, D. Graf, A. F. Young, and C. R. Dean, Tuning superconductivity in twisted bilayer graphene, Science **363**, 1059 (2019).

[9] A. L. Sharpe, E. J. Fox, A. W. Barnard, J. Finney, K. Watanabe, T. Taniguchi, M. A. Kastner, and D. Goldhaber-Gordon, Emergent ferromagnetism near three-quarters filling in twisted bilayer graphene, Science **365**, 605 (2019).

[10] X. Lu, P. Stepanov, W. Yang, M. Xie, M. A. Aamir, I. Das, C. Urgell, K. Watanabe, T. Taniguchi, G. Zhang, A. Bachtold, A. H. MacDonald, and D. K. Efetov, Superconductors, orbital magnets and correlated states in magic-angle bilayer graphene, Nature (London) **574**, 653 (2019).

[11] Y. Jiang, X. Lai, K. Watanabe, T. Taniguchi, K. Haule, J. Mao, and E. Y. Andrei, Charge order and broken rotational symmetry in magic-angle twisted bilayer graphene, Nature (London) **573**, 91 (2019).

[12] M. Serlin, C. L. Tschirhart, H. Polshyn, Y. Zhang, J. Zhu, K. Watanabe, T. Taniguchi, L. Balents, and A. F. Young, Intrinsic quantized anomalous Hall effect in a moiré heterostructure, Science **367**, 900 (2020).

[13] X. Liu, Z. Hao, E. Khalaf, J. Y. Lee, Y. Ronen, H. Yoo, D. Haei Najafabadi, K. Watanabe, T. Taniguchi, A. Vishwanath, and P. Kim, Tunable spin-polarized correlated states in twisted double bilayer graphene, Nature (London) **583**, 221 (2020).

[14] E. Y. Andrei and A. H. MacDonald, Graphene bilayers with a twist, Nat. Mater. **19**, 1265 (2020).

[15] Z. Zhang, Y. Wang, K. Watanabe, T. Taniguchi, K. Ueno, E. Tutuc, and B. J. LeRoy, Flat bands in twisted bilayer transition metal dichalcogenides, Nat. Phys. **16**, 1093 (2020).

[16] E. C. Regan, D. Wang, C. Jin, M. I. B. Utama, B. Gao, X. Wei, S. Zhao, W. Zhao, Z. Zhang, K. Yumigeta *et al.*, Mott and generalized Wigner crystal states in WSe_2/WS_2 moiré superlattices, Nature (London) **579**, 359 (2020).

[17] Y. Tang, L. Li, T. Li, Y. Xu, S. Liu, K. Barmak, K. Watanabe, T. Taniguchi, A. H. MacDonald, J. Shan *et al.*, Simulation of Hubbard model physics in WSe_2/WS_2 moiré superlattices, Nature (London) **579**, 353 (2020).

[18] J. M. B. Lopes dos Santos, N. M. R. Peres, and A. H. Castro Neto, Graphene bilayer with a twist: Electronic structure, Phys. Rev. Lett. **99**, 256802 (2007).

[19] R. Bistritzer and A. H. MacDonald, Moiré bands in twisted double-layer graphene, Proc. Natl. Acad. Sci. USA **108**, 12233 (2011).

[20] G. Tarnopolsky, A. J. Kruchkov, and A. Vishwanath, Origin of magic angles in twisted bilayer graphene, Phys. Rev. Lett. **122**, 106405 (2019).

[21] Y. Fu, E. J. König, J. H. Wilson, Y.-Z. Chou, and J. H. Pixley, Magic-angle semimetals, npj Quantum Mater. **5**, 71 (2020).

[22] S. Carr, D. Massatt, S. Fang, P. Cazeaux, M. Luskin, and E. Kaxiras, Twistronics: Manipulating the electronic properties of two-dimensional layered structures through their twist angle, Phys. Rev. B **95**, 075420 (2017).

[23] L. Balents, C. R. Dean, D. K. Efetov, and A. F. Young, Superconductivity and strong correlations in moiré flat bands, Nat. Phys. **16**, 725 (2020).

[24] J. Kang and O. Vafek, Strong coupling phases of partially filled twisted bilayer graphene narrow bands, Phys. Rev. Lett. **122**, 246401 (2019).

[25] J. Y. Lee, E. Khalaf, S. Liu, X. Liu, Z. Hao, P. Kim, and A. Vishwanath, Theory of correlated insulating behaviour and spin-triplet superconductivity in twisted double bilayer graphene, Nat. Commun. **10**, 5333 (2019).

[26] C. Repellin, Z. Dong, Y.-H. Zhang, and T. Senthil, Ferromagnetism in narrow bands of moiré superlattices, Phys. Rev. Lett. **124**, 187601 (2020).

[27] D. D. Vu and S. Das Sarma, Moiré versus Mott: Incommensuration and interaction in one-dimensional bichromatic lattices, Phys. Rev. Lett. **126**, 036803 (2021).

[28] H. C. Po, L. Zou, A. Vishwanath, and T. Senthil, Origin of Mott insulating behavior and superconductivity in twisted bilayer graphene, Phys. Rev. X **8**, 031089 (2018).

[29] H. C. Po, L. Zou, T. Senthil, and A. Vishwanath, Faithful tight-binding models and fragile topology of magic-angle bilayer graphene, Phys. Rev. B **99**, 195455 (2019).

[30] L. Zou, H. C. Po, A. Vishwanath, and T. Senthil, Band structure of twisted bilayer graphene: Emergent symmetries, commensurate approximants, and Wannier obstructions, Phys. Rev. B **98**, 085435 (2018).

[31] J. Kang and O. Vafek, Symmetry, maximally localized Wannier states, and a low-energy model for twisted bilayer graphene narrow bands, Phys. Rev. X **8**, 031088 (2018).

[32] F. Guinea and N. R. Walet, Electrostatic effects, band distortions, and superconductivity in twisted graphene bilayers, Proc. Natl. Acad. Sci. USA **115**, 13174 (2018).

[33] Y.-H. Zhang and T. Senthil, Bridging Hubbard model physics and quantum Hall physics in trilayer graphene/*h*-BN moiré superlattice, Phys. Rev. B **99**, 205150 (2019).

[34] Z. Song, Z. Wang, W. Shi, G. Li, C. Fang, and B. A. Bernevig, All magic angles in twisted bilayer graphene are topological, Phys. Rev. Lett. **123**, 036401 (2019).

[35] T. Cea and F. Guinea, Band structure and insulating states driven by Coulomb interaction in twisted bilayer graphene, Phys. Rev. B **102**, 045107 (2020).

[36] B. A. Bernevig, Z.-D. Song, N. Regnault, and B. Lian, Twisted bilayer graphene. III. Interacting Hamiltonian and exact symmetries, Phys. Rev. B **103**, 205413 (2021).

[37] B. Lian, Z.-D. Song, N. Regnault, D. K. Efetov, A. Yazdani, and B. A. Bernevig, Twisted bilayer graphene. IV. Exact insulator ground states and phase diagram, Phys. Rev. B **103**, 205414 (2021).

[38] D. N. Basov and T. Timusk, Electrodynamics of high-T_c superconductors, Rev. Mod. Phys. **77**, 721 (2005).

[39] M. Liao, Y. Zhu, J. Zhang, R. Zhong, J. Schneeloch, G. Gu, K. Jiang, D. Zhang, X. Ma, and Q.-K. Xue, Superconductor–insulator transitions in exfoliated $Bi_2Sr_2CaCu_2O_8 + \delta$ flakes, Nano Lett. **18**, 5660 (2018).

[40] Y. Yu, L. Ma, P. Cai, R. Zhong, C. Ye, J. Shen, G. D. Gu, X. H. Chen, and Y. Zhang, High-temperature superconductivity in monolayer $Bi_2Sr_2CaCu_2O_{8+\delta}$, Nature (London) **575**, 156 (2019).

[41] S. Y. Frank Zhao, N. Poccia, M. G. Panetta, C. Yu, J. W. Johnson, H. Yoo, R. Zhong, G. D. Gu, K. Watanabe, T. Taniguchi, S. V. Postolova, V. M. Vinokur, and P. Kim, Sign-reversing Hall effect in atomically thin high-temperature $Bi_{2.1}Sr_{1.9}CaCu_{2.0}O_{8+\delta}$ superconductors, Phys. Rev. Lett. **122**, 247001 (2019).

[42] L. Balents, General continuum model for twisted bilayer graphene and arbitrary smooth deformations, SciPost Phys. **7**, 048 (2019).

[43] P. A. Volkov, J. H. Wilson, K. P. Lucht, and J. H. Pixley, Current- and field-induced topology in twisted nodal superconductors, Phys. Rev. Lett. **130**, 186001 (2023).

[44] P. A. Volkov, J. H. Wilson, K. P. Lucht, and J. H. Pixley, Magic angles and correlations in twisted nodal superconductors, Phys. Rev. B **107**, 174506 (2023).

[45] Z. Yang, S. Qin, Q. Zhang, C. Fang, and J. Hu, $\pi/2$-Josephson junction as a topological superconductor, Phys. Rev. B **98**, 104515 (2018).

[46] O. Can, T. Tummuru, R. P. Day, I. Elfimov, A. Damascelli, and M. Franz, High-temperature topological superconductivity in twisted double-layer copper oxides, Nat. Phys. **17**, 519 (2021).

[47] M. Sigrist, Time-reversal symmetry breaking states in high-temperature superconductors, Prog. Theor. Phys. **99**, 899 (1998).

[48] S. F. Zhao, X. Cui, P. A. Volkov, H. Yoo, S. Lee, J. A. Gardener, A. J. Akey, R. Engelke, Y. Ronen, R. Zhong *et al.*, Time-reversal symmetry breaking superconductivity between twisted cuprate superconductors, Science **382**, 1422 (2023).

[49] M. Martini, Y. Lee, T. Confalone, S. Shokri, C. N. Saggau, D. Wolf, G. Gu, K. Watanabe, T. Taniguchi, D. Montemurro *et al.*, Twisted cuprate van der Waals heterostructures with controlled Josephson coupling, Mater. Today **67**, 106 (2023).

[50] Y. Lee, M. Martini, T. Confalone, S. Shokri, C. N. Saggau, D. Wolf, G. Gu, K. Watanabe, T. Taniguchi, D. Montemurro *et al.*, Encapsulating high-temperature superconducting twisted van der Waals heterostructures blocks detrimental effects of disorder, Adv. Mater. **35**, 2209135 (2023).

[51] Q. Li, Y. N. Tsay, M. Suenaga, R. A. Klemm, G. D. Gu, and N. Koshizuka, $Bi_2Sr_2CaCu_2O_{8+\delta}$ bicrystal *c*-axis twist Josephson junctions: A new phase-sensitive test of order parameter symmetry, Phys. Rev. Lett. **83**, 4160 (1999).

[52] Y. Takano, T. Hatano, A. Fukuyo, A. Ishii, M. Ohmori, S. Arisawa, K. Togano, and M. Tachiki, *d*-like symmetry of the order parameter and intrinsic Josephson effects in $Bi_2Sr_2CaCu_2O_{8+\delta}$ cross-whisker junctions, Phys. Rev. B **65**, 140513(R) (2002).

[53] Y. Zhu, M. Liao, Q. Zhang, H.-Y. Xie, F. Meng, Y. Liu, Z. Bai, S. Ji, J. Zhang, K. Jiang, R. Zhong, J. Schneeloch, G. Gu, L. Gu, X. Ma, D. Zhang, and Q.-K. Xue, Presence of *s*-wave pairing in Josephson junctions made of twisted ultrathin $Bi_2Sr_2CaCu_2O_{8+x}$ flakes, Phys. Rev. X **11**, 031011 (2021).

[54] A. Bille, R. A. Klemm, and K. Scharnberg, Models of c-axis twist Josephson tunneling, Phys. Rev. B **64**, 174507 (2001).

[55] R. A. Klemm, The phase-sensitive c-axis twist experiments on $Bi_2Sr_2CaCu_2O_8 + \delta$ and their implications, Philos. Mag. **85**, 801 (2005).

[56] P. A. Volkov, E. Lantagne-Hurtubise, T. Tummuru, S. Plugge, J. H. Pixley, and M. Franz, Josephson diode effects in twisted nodal superconductors, Phys. Rev. B **109**, 094518 (2024).

[57] T. Tummuru, S. Plugge, and M. Franz, Josephson effects in twisted cuprate bilayers, Phys. Rev. B **105**, 064501 (2022).

[58] K. P. Lucht, J. Pixley, and P. A. Volkov, Topological superconductivity in twisted flakes of nodal superconductors, arXiv:2312.13367.

[59] K. Maki and S. Haas, c-axis Josephson tunneling in $d_{x^2-y^2}$-wave superconductors, Phys. Rev. B **67**, 020510(R) (2003).

[60] Y. Zhu, H. Wang, Z. Wang, S. Hu, G. Gu, J. Zhu, D. Zhang, and Q.-K. Xue, Persistent Josephson tunneling between $Bi_2Sr_2CaCu_2O_{8+x}$ flakes twisted by 45° across the superconducting dome, Phys. Rev. B **108**, 174508 (2023).

[61] R. Kleiner, F. Steinmeyer, G. Kunkel, and P. Müller, Intrinsic Josephson effects in $Bi_2Sr_2CaCu_2O_8$ single crystals, Phys. Rev. Lett. **68**, 2394 (1992).

[62] R. Kleiner and P. Müller, Intrinsic Josephson effects in high-T_c superconductors, Phys. Rev. B **49**, 1327 (1994).

[63] A. A. Golubov, M. Y. Kupriyanov, and E. Il'ichev, The current-phase relation in Josephson junctions, Rev. Mod. Phys. **76**, 411 (2004).

[64] Y. Tanaka and S. Kashiwaya, Theory of the Josephson effect in d-wave superconductors, Phys. Rev. B **53**, R11957 (1996).

[65] S. Kashiwaya and Y. Tanaka, Tunnelling effects on surface bound states in unconventional superconductors, Rep. Prog. Phys. **63**, 1641 (2000).

[66] R. S. Markiewicz, S. Sahrakorpi, M. Lindroos, H. Lin, and A. Bansil, One-band tight-binding model parametrization of the high-T_c cuprates including the effect of k_z dispersion, Phys. Rev. B **72**, 054519 (2005).

[67] O. Andersen, A. Liechtenstein, O. Jepsen, and F. Paulsen, LDA energy bands, low-energy Hamiltonians, t', t'', $t^{\perp}$ (k), and $J^{\perp}$, J. Phys. Chem. Solids **56**, 1573 (1995), proceedings of the Conference on Spectroscopies in Novel Superconductors.

[68] V. Ambegaokar and A. Baratoff, Tunneling between superconductors, Phys. Rev. Lett. **10**, 486 (1963).

[69] V. Ambegaokar and A. Baratoff, Tunneling between superconductors, Phys. Rev. Lett. **11**, 104 (1963).

[70] N. Poccia, S. Y. F. Zhao, H. Yoo, X. Huang, H. Yan, Y. S. Chu, R. Zhong, G. Gu, C. Mazzoli, K. Watanabe, T. Taniguchi, G. Campi, V. M. Vinokur, and P. Kim, Spatially correlated incommensurate lattice modulations in an atomically thin high-temperature $Bi_{2.1}Sr_{1.9}CaCu_{2.0}O_{8+y}$ superconductor, Phys. Rev. Mater. **4**, 114007 (2020).

[71] $I_c^2(\theta = 0) \propto t^2 k_F / v_F$; $I_c^4(\theta = 45^\circ) \sim t^4 / v_F^2 \Delta$ (the integral is accumulated close to the point where Fermi surfaces cross).

[72] A. C. Yuan, Y. Vituri, E. Berg, B. Spivak, and S. A. Kivelson, Inhomogeneity-induced time-reversal symmetry breaking in cuprate twist junctions, Phys. Rev. B **108**, L100505 (2023).

[73] C. S. Owen and D. J. Scalapino, Vortex structure and critical currents in Josephson junctions, Phys. Rev. **164**, 538 (1967).

[74] A. Barone and G. Paterno, *Physics and Applications of the Josephson Effect* (Wiley Online Library, New York, 1982), Vol. 1.

[75] A. Barone, W. J. Johnson, and R. Vaglio, Current flow in large Josephson junctions, J. Appl. Phys. **46**, 3628 (1975).

[76] Y. I. Latyshev, J. E. Nevelskaya, and P. Monceau, Dimensional crossover for intrinsic dc Josephson effect in $Bi_2Sr_2CaCu_2O_8$ 2212 single crystal whiskers, Phys. Rev. Lett. **77**, 932 (1996).

[77] L. N. Bulaevskii, J. R. Clem, and L. I. Glazman, Fraunhofer oscillations in a multilayer system with Josephson coupling of layers, Phys. Rev. B **46**, 350 (1992).

[78] H. Enriquez, N. Bontemps, A. A. Zhukov, D. V. Shovkun, M. R. Trunin, A. Buzdin, M. Daumens, and T. Tamegai, Penetration of Josephson vortices and measurement of the c-axis penetration depth in $Bi_2Sr_2CaCu_2O_{8+\delta}$: Interplay of Josephson coupling, surface barrier, and defects, Phys. Rev. B **63**, 144525 (2001).

[79] M. V. Fistul and G. F. Giuliani, Magnetic field dependence of the critical current of a layered superconductor, Physica C **230**, 9 (1994).

[80] S.-F. Lee, D. C. Morgan, R. J. Ormeno, D. M. Broun, R. A. Doyle, J. R. Waldram, and K. Kadowaki, a-b plane microwave surface impedance of a high-quality $Bi_2Sr_2CaCu_2O_8$ single crystal, Phys. Rev. Lett. **77**, 735 (1996).

[81] T. Senthil, J. B. Marston, and M. P. A. Fisher, Spin quantum Hall effect in unconventional superconductors, Phys. Rev. B **60**, 4245 (1999).

[82] M. Tinkham, *Introduction to Superconductivity* (Dover, New York, 1996).

[83] E. Goldobin, D. Koelle, R. Kleiner, and A. Buzdin, Josephson junctions with second harmonic in the current-phase relation: properties of ϕ junctions, Phys. Rev. B **76**, 224523 (2007).

[84] H. Sellier, C. Baraduc, F. Lefloch, and R. Calemczuk, Half-integer shapiro steps at the 0-π crossover of a ferromagnetic Josephson junction, Phys. Rev. Lett. **92**, 257005 (2004).

[85] G. L. Alfimov and A. F. Popkov, Magnetic vortices in a distributed Josephson junction with electrodes of finite thickness, Phys. Rev. B **52**, 4503 (1995).